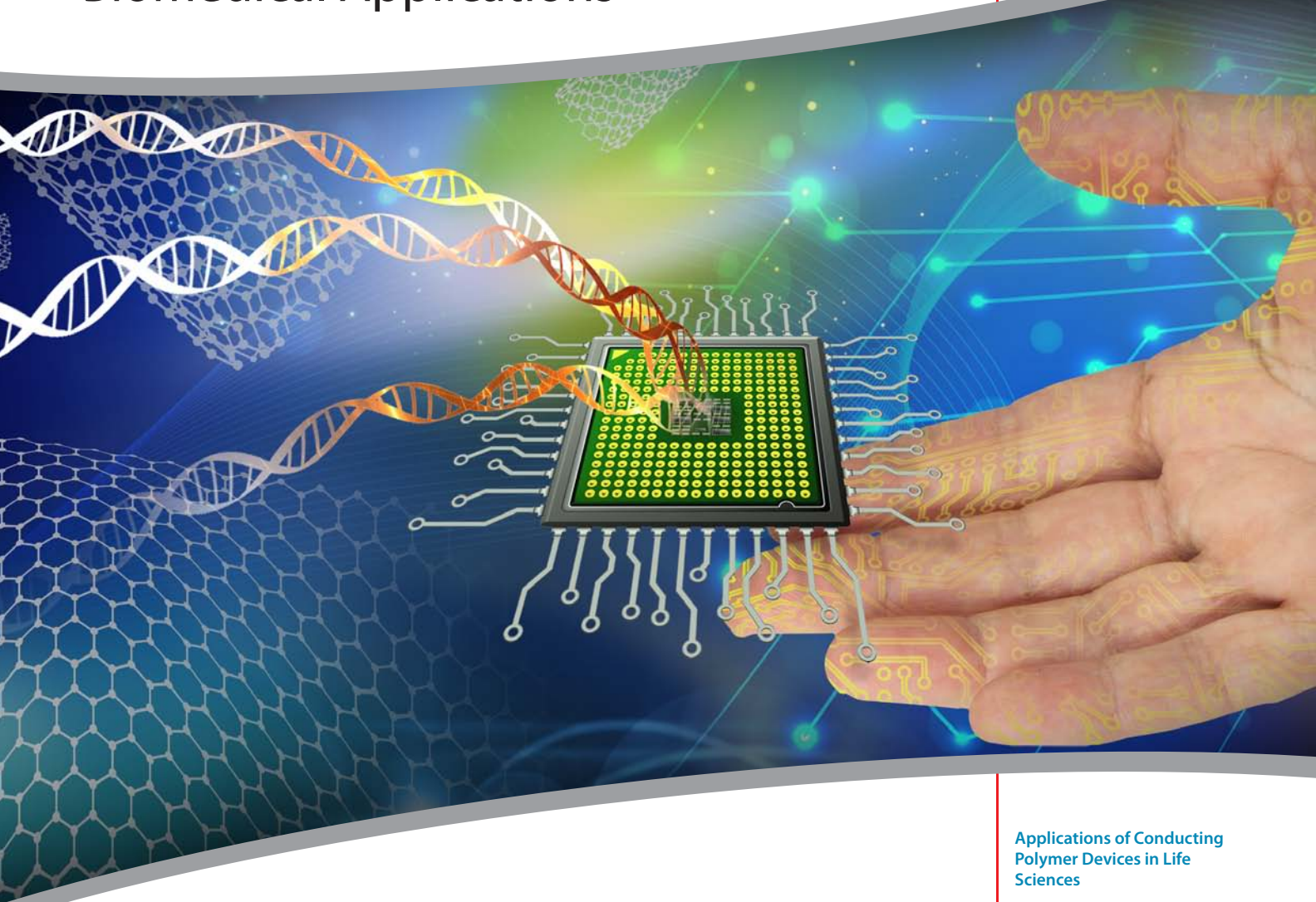


Material Matters™

Volume 8, Number 1

ALDRICH
Materials Science

Materials for Bioelectronic and Biomedical Applications



Transmitting New Ideas

Applications of Conducting
Polymer Devices in Life
Sciences

Flexible Organic Transistors for
Biomedical Applications

Sorting Carbon Nanotubes and
Their Biological Applications

Graphene in Biotechnology

SIGMA-ALDRICH®

Introduction

Welcome to the first issue of *Material Matters*™ for 2013 focusing on biological and medical applications of electronic and nanomaterials. Bioelectronics interfaces electronics and biology with research efforts that cross disciplines such as chemistry, biology, physics, electrical engineering, and materials science. Organic electronic and carbon nanomaterials are highly desirable for application in bioelectronics research due to their biocompatible and flexible nature. Applications include wearable electronics (e.g. sensors and actuators) and more recently implantable electronics. It is reasonable to believe that these human-friendly electronic materials will play even more important roles in our daily life, from safety, disease diagnostics, and even life-sustaining technologies.

In our first article Professor George Malliaras and Professor Róisín Owens (Ecole Nationale Supérieure des Mines, France) and their collaborators provide two examples of innovative organic bioelectronic devices: electrocorticography arrays and organic electrochemical transistors comprised of conducting polymers. Owing to the intrinsic conductivity and the conformability of polymeric molecules, both devices can be used to record subtle signals inside living cells, such as human brain and cancer cells, with enhanced diagnostic capabilities.

In the second article, Professor Tsuyoshi Sekitani and Professor Takao Someya (University of Tokyo, Japan) describe the development of heat-resistant, flexible, organic thin-film transistors (TFTs) utilizing DNTT. Remarkably, the DNTT-based TFT demonstrates tolerance to harsh medical sterilization conditions, without reducing its high mobility performance. Moreover, these TFTs remain flexible enabling the design of foldable transistors for medical catheter that measures spatial distribution of pressure.

Professor Sang-Yong Ju (Yonsei University, Korea) in our third article reviews recent methodological advances in purifying carbon nanotubes (CNTs) according to their physical properties. Cutting-edge biological applications such as bioimaging, drug/gene delivery, and cancer therapy using these well sorted CNTs with defined structure, electronic type, chirality, length and handedness are also described. It is anticipated that CNTs will find extensive utility in bioelectronics devices and other biomedical applications. For example, in *Your Material Matters*, Professor Wei Chen (Central Oklahoma University, USA) highlights some early encouraging clinical results on treatment of certain types of cancer using very high purity, controlled chirality, small diameter single-walled CNTs.

Finally, Dr. Amaia Zurutuza Elorza and Dr. Alba Centeno (Graphenea S.A., Spain) discuss a new wonder material, Graphene, and focus on its potential biomedical and bioelectronic applications. Graphene displays incredible properties such as high electron mobility and thermal conductivity, transparency, flexibility, and impermeability. Additional properties such as biocompatibility, physiological solubility, stability, and capability of loading or conjugating different type of compounds to graphene are currently the focus of extensive research to unleash the potential of this truly super material.

Each article in this issue is accompanied by the corresponding Aldrich Materials Science products which will facilitate research efforts to fabricate high performance bioelectronic devices. For a comprehensive library of products and associated technical information, please visit us at aldrich.com/matsci. We welcome your comments, questions, new product suggestions, and custom requests to matsci@sial.com.

About Our Cover

Rapid technological advances in electronics and life science allow today's organic electronic and nanomaterials to advance the field of *Bio-Electronics*. The cover art illustrates a "gene chip" containing thousands of DNA microarrays which can be used for disease screening, diagnostics, progression monitoring, and even disease treatment. Aldrich Materials Science is proud to help enable this cutting-edge technology with a large variety of innovative materials.



Yong Zhang, Ph.D.
Aldrich Materials Science

Material Matters™

Vol. 8, No. 1

Aldrich Materials Science
Sigma-Aldrich Co. LLC
6000 N. Teutonia Ave.
Milwaukee, WI 53209, USA

To Place Orders

Telephone 800-325-3010 (USA)
FAX 800-325-5052 (USA)

International customers, contact your local Sigma-Aldrich office (sigma-aldrich.com/worldwide-offices).

Customer & Technical Services

Customer Inquiries 800-325-3010
Technical Service 800-325-5832
SAFC® 800-244-1173
Custom Synthesis 800-244-1173
Flavors & Fragrances 800-227-4563
International 314-771-5765
24-Hour Emergency 314-776-6555
Safety Information sigma-aldrich.com/safetycenter
Website sigma-aldrich.com
Email aldrich@sial.com

Subscriptions

Request your FREE subscription to *Material Matters*:

Phone 800-325-3010 (USA)
Mail Attn: Marketing Communications
Aldrich Chemical Co., Inc
Sigma-Aldrich Co. LLC
P.O. Box 2988
Milwaukee, WI 53201-2988
Website aldrich.com/mm
Email sams-usa@sial.com

Material Matters (ISSN 1933-9631) is a publication of Aldrich Chemical Co., Inc. Aldrich is a member of the Sigma-Aldrich Group.

Online Versions



Explore previous editions of
Material Matters. Visit
aldrich.com/materialmatters

©2013 Sigma-Aldrich Co. LLC. All rights reserved.
SIGMA, SAFC, SIGMA-ALDRICH, ALDRICH, and SUPELCO are trademarks of Sigma-Aldrich Co. LLC, registered in the US and other countries. FLUKA is a trademark of Sigma-Aldrich GmbH, registered in the US and other countries. *Material Matters* is a trademark of Sigma-Aldrich Co. LLC. Sigma brand products are sold through Sigma-Aldrich, Inc. Purchaser must determine the suitability of the product(s) for their particular use. Additional terms and conditions may apply. Please see product information on the Sigma-Aldrich website at www.sigmaaldrich.com and/or on the reverse side of the invoice or packing slip.

Table of Contents

Articles

Applications of Conducting Polymer Devices in Life Sciences	2
Flexible Organic Transistors for Biomedical Applications	8
Sorting Carbon Nanotubes and Their Biological Applications	18
Graphene in Biotechnology	25

Featured Products

PEDOT Materials.	4
<i>(A selection of PEDOT:PSS and other PEDOT dispersions)</i>	
Polyaniline (PANI)	6
<i>(A list of conducting polyaniline emeraldine salts)</i>	
Polypyrrole (PPy)	6
<i>(A list of doped polypyrrole homopolymers and a copolymer)</i>	
Polythiophene (PT)	6
<i>(A list of poly(3-alkylthiophene) (P3AT))</i>	
Popular Cell Culture Lines.	7
<i>(A selection of Sigma® Life Science cell culture line products)</i>	
Organic Semiconductors	11
<i>(A selection of p- and n-type small molecular and polymeric organic semiconductors for flexible organic transistors)</i>	
Phosphonic Acids for Self-assembly	16
<i>(A list of mono- and diphosphonic acids)</i>	
Single-walled Carbon Nanotubes (SWNT)	22
<i>(A list of SWNT with high purity produced by different methods)</i>	
Double-walled Carbon Nanotubes (DWNT)	23
<i>(A list of DWNT with high purity produced by different methods)</i>	
Multi-walled Carbon Nanotubes (MWNT)	23
<i>(A list of MWNT with high purity produced by different methods)</i>	
Functionalized Nanotubes	23
<i>(A list of functionalized nanotubes based on SWNT and MWNT)</i>	
Graphene	29
<i>(A list of monolayer graphene films on different substrates)</i>	
Graphene Oxides	30
<i>(A list of graphene oxide dispersion and flakes)</i>	
Dyes for Biosensing.	30
<i>(A selection of laser, chemiluminescent, photochromic and thermochromic dyes)</i>	
Biotium Kits	33
<i>(A list of Sigma® Life Science Biotium kits for antibody labeling)</i>	

Your Materials Matter



Bryce P. Nelson

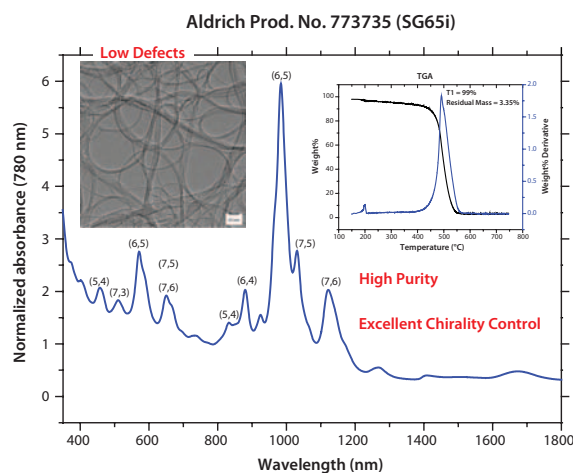
Bryce P. Nelson, Ph.D.
Aldrich® Materials Science Initiative Lead

We welcome fresh product ideas from you. Do you have a material or compound you wish to see in our Aldrich® Materials Science line? If it is needed to accelerate your research, it matters. Send your suggestion to matsci@sial.com for consideration.

Professor Wei R. Chen (Central Oklahoma University, USA) suggested we offer very high purity, excellent chirality control, and small diameter Single-walled Carbon Nanotubes (SWNTs) (SG65i, **Aldrich Product No. 773735**) produced by the patented CoMoCAT® process.¹ These SWNTs function as drug delivery vehicles, effectively penetrating the walls of cancer cells, and can be attached to an immunological stimulant such as glycated chitosan. Combined with different treatment modalities, the efficacy of cancer treatment in pre-clinical studies dramatically increases, particularly when using a synchronized photoimmunological interaction.²⁻³ Early research results are very encouraging: CoMoCAT SWNTs have great potential for medical applications.

References

- Resasco D. E.; Alvarez, W. E.; Pompeo, F.; Balzano, L.; Herrera, J. E.; Kitiyanan, B.; Borgna, A. J. *Nanopart. Res.* **2002**, 4, 131-136.
- Zhou, F.; Xing, D.; Wu, B.; Wu, S.; Ou, Z. and Chen, W. R. *Nano Letters* **2010**, 10, 1677-1681.
- Zhou, F.; Wu, S.; Song, S.; Chen, W. R.; Resasco D. E. and Xing, D. *Biomaterials* **2012**, 33, 3235-42.



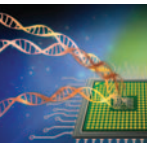
Carbon nanotube, single-walled

Single wall carbon nanotube; SWNT; SWCNT
[308068-56-6]

► **SWE^{NT}® SG 65i**
(6,5) chirality, ≥93% (carbon as SWNT)

CoMoCAT® Catalytic Chemical Vapor Deposition (CVD) Method
diameter 0.7-0.9 nm (by fluorescence)

773735-250MG	250 mg
773735-1G	1 g



Applications of Conducting Polymer Devices in Life Sciences



Leslie H. Jimison¹, Dion Khodagholy¹, Thomas Doublet^{1,2}, Christophe Bernard², George G. Malliaras¹, and Róisín M. Owens¹
¹Department of Bioelectronics, Ecole Nationale Supérieure des Mines CMP-EMSE, MOC, 880 route de Mimet, 13541 Gardanne, France (www.bel.emse.fr)
²Institut de Neurosciences des Systèmes, Inserm UMR1106, Aix-Marseille Université Faculté de Médecine, 27 Boulevard Jean Moulin, 13005 Marseille, France

Introduction

The application of conducting polymers at the interface with biology is an exciting new trend in organic electronics research.¹⁻³ The nascent field of organic bioelectronics involves the coupling of organic electronic devices (such as electrodes and transistors) with biological systems, in an effort to bridge the biotic/abiotic interface. There are a number of unique characteristics of conducting polymers that make them well-suited for integration with living systems:

1. Mixed conduction of both electronic and ionic charge carriers is a major advantage for communication with biological systems, which rely heavily on ionic fluxes.
2. Conducting polymers form ideal interfaces with electrolyte solutions that lack native oxides and dangling bonds.
3. These van der Waals bonded solids have “soft” mechanical properties that better match those of the majority of biological tissues, leading to a lower mechanical mismatch in implanted devices.
4. As in other applications for conducting polymers, solution processing of these materials facilitates easy fabrication and unique form factors.

Solution-processibility becomes especially important when designing flexible devices or inexpensive single-use sensors. These characteristics combine to provide a new toolbox for interfacing electronics with biology, and more importantly, solving problems related to biodiagnostics and treatment of biological dysfunction.

Herein we discuss two examples of conducting polymers at the interface with life sciences, showcasing the versatility and multi-functionality of these materials. The first is the development of conducting polymer electrodes that provide high-quality recordings of brain activity. The electrodes are fabricated on a highly conformable array, allowing for intimate contact with the surface of the brain. The second introduces an organic electronic cell-based sensor, where living tissue acts as the broad first line of defense against a range of toxins. This sensor has a direct application in diagnostics and understanding the mechanisms of drug delivery.

Poly(3,4-ethylenedioxythiophene):poly(styrenesulfonate) (PEDOT:PSS) in Bioelectronics

Due to the versatility of polymer synthesis, there exists a large library of conducting polymer systems. In recent years, PEDOT:PSS has emerged as a champion material in the field of bioelectronics. The p-conjugation gives PEDOT its semiconducting properties, while the PSS acts as a p-type dopant and raises the room temperature electrical conductivity to high levels (100 S/cm, even up to 1,000 S/cm with proper optimization). Both of the examples discussed in this article are based on commercially available PEDOT:PSS aqueous dispersions ([Aldrich Product Nos. 739332, 739324, 739316 and 768642](#)).

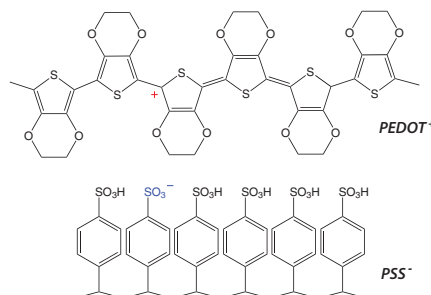


Figure 1. Chemical structure of PEDOT⁺ and PSS⁻. The fixed negative charges on the PSS chain are balanced by polarons existing on the PEDOT chain, giving rise to enhanced electronic conductivity.

Applications in Brain Recordings

Electronic devices that interface with living tissue have become a necessity in clinics to improve diagnoses and treatments. One such example is electrocorticography (ECoG) electrode arrays, which are increasingly used for functional mapping of cognitive processes before certain types of brain surgery (e.g., tumors), for diagnostic purposes (e.g., epilepsy)⁵ and for brain-machine interfaces, an assistive technology for people with severe motor disabilities.⁶ These electrodes must conform to the curvilinear shapes of the brain and form high-quality electrical contacts. Thin sheets of polymeric materials with metal electrodes are traditionally used for this purpose.⁷

Using microfabrication techniques, our group prepared ECoG arrays with conducting polymer electrodes.⁸ A micrograph of the electrodes is shown in **Figure 2A**. The arrays consisted of a parylene substrate, gold contact pads and interconnects, and parylene insulation. A PEDOT:PSS film was deposited in appropriate holes in the insulation layer, defining the electrodes. The total thickness of the arrays was 4 μm, yet the electrode arrays had adequate mechanical strength to be self-supporting and to be manipulated by a surgeon. **Figure 2B** shows a micrograph of an array conforming to the midrib of a small leaf.

Arrays were placed on the somatosensory cortex of anaesthetized rats. The recordings were done after the addition of bicuculline ([Sigma Product No. 14340](#)), a GABA_A receptor antagonist that enables the genesis of sharp-wave events which mimic epileptic spikes.⁹ The recordings were validated against a commercial implantable electrode. **Figure 2C** shows that the power spectrum of a recording from a PEDOT:PSS electrode exhibits the typical 1/f property of the ECoG spectrum, with good definition of the 1–10 Hz and the 30 Hz bands. These bands are the dominant ones during bicuculline-triggered sharp-wave events. It should be noted that gold electrodes of similar size did not yield adequate recordings, due to the fact that their interface

impedance was much higher. Thus, PEDOT:PSS electrodes were found to outperform traditional metal electrodes, which highlights the importance of incorporating conducting polymers in a highly conformable electrode array format.

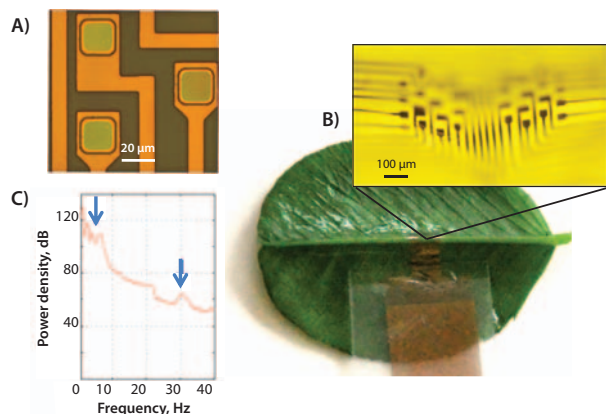


Figure 2. A) Micrograph of the array showing a detailed view of three electrodes. B) An electrode array is shown to conform to the midrib of a small leaf. C) Power spectrum of representative recording with a PEDOT:PSS electrode. The blue arrows indicate the 1–10 Hz and the 30 Hz bands.

Applications in Whole Cell Biosensors

We have demonstrated the direct integration of barrier tissue with an organic electrochemical transistor (OECT). The result is a cell-based sensor for monitoring barrier tissue integrity *in situ* with high sensitivity and temporal resolution.¹⁰ Barrier tissue is comprised of tightly packed layers of epithelial cells. Examples in the body include the gastrointestinal (GI) tract and the blood brain barrier. Acting as the first layer of defense, these cell layers help to block the passage of toxins and pathogens, but allow the passage of ions, water, and nutrients. The ability of barrier tissue to impose such highly regulated transport arises from the presence of protein complexes at the border between neighboring cells, including the tight junction (TJ) and the adherens junction (AJ).¹¹ When these cell-cell seals are compromised, the regulated transport is affected as well. Thus, disruptions in barrier tissue integrity are often indicative of the presence of toxins and pathogens. The work presented here uses the Caco-2 cell line ([Sigma Product No. 86010202](#)), derived from a human colon cancer. When grown on a permeable membrane, these cells differentiate into an appropriate *in vitro* model for the gastrointestinal tract, characterized by localized junctional proteins, low permeability to tracer molecules, and high transepithelial electrical resistance (TER).¹²

The sensor presented here relies on the operating mechanism of an organic electrochemical transistor (OECT).¹³ An OECT consists of a conducting polymer (PEDOT:PSS) channel in contact with an electrolyte (here, cell culture medium). A gate electrode (Ag/AgCl) is immersed in the electrolyte, and source and drain contacts at either side of the transistor channel measure the drain current (I_D). On application of a positive gate voltage (V_G), cations from the electrolyte drift into the PEDOT:PSS channel, de-doping the conducting polymer and decreasing the drain current (I_D). The ionic flux from the electrolyte into the polymer film determines the speed at which the drain current changes. By integrating the cell layer into the OECT architecture as shown in **Figure 3A**, the transient OECT behavior is directly correlated with the ionic flux allowed through the barrier tissue. A lower ionic flux results in a slower I_D response and vice versa. Thus, changes in the barrier tissue integrity are reflected in changes in I_D transient response.

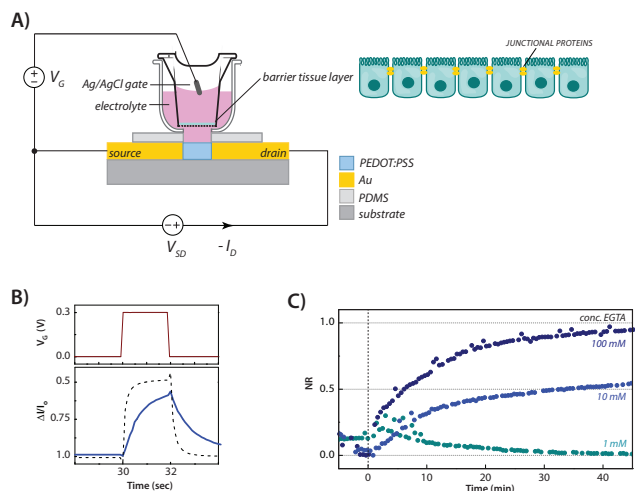
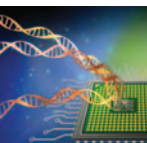


Figure 3. A) Architecture of an OECT integrated with barrier tissue layer; tissue is supported on a permeable membrane. The illustration on the right shows tightly packed epithelial cells with junctional proteins that regulate transport. B) OECT characteristics, showing a V_G pulse (top) and normalized drain current, $\Delta I/I_0$ (bottom), when healthy cells are present (solid blue) and when no cells are present (dashed black). A reduction in ionic flux caused by the presence of a barrier tissue layer slows device response time ($V_G = 0.3$ V). C) Normalized Response (NR) calculated from OECT modulation on addition of varying concentrations of ethylene glycol-bis(2-aminoethyl ether)-*N,N,N',N'*-tetraacetic acid (EGTA), as shown. EGTA was added at time=0. NR=0 refers to observed modulation when a healthy barrier layer is present, and NR=1 refers to observed modulation when barrier properties are destroyed: progression from 0 to 1 indicates barrier tissue disruption.

We used the OECT barrier tissue sensor to monitor the effect of ethylene glycol-bis(2-aminoethylether)-*N,N,N',N'*-tetraacetic acid (EGTA), a specific calcium chelator, on barrier tissue integrity ([Sigma-Aldrich Product Nos. E3889](#) and [03777](#)). The junctional protein complexes existing between cells are dynamic in nature: changes in the extracellular environment, including calcium concentration, affect their assembly and function. When the extracellular calcium levels are too low, some junctional proteins are internalized.¹⁴ EGTA has been shown previously to effectively modify extracellular environment, leading to an increase in paracellular diffusion across barrier tissue.¹⁵ On introduction of 1 mM EGTA to the basolateral side of the barrier tissue layer, we observe negligible changes in the response of the OECT, indicating no disruption of barrier properties. On addition of 10 and 100 mM EGTA, we observe a concentration-dependent effect, with the presence of 100 mM EGTA destroying barrier integrity within 45 minutes. With the OECT sensor, we are able to monitor the evolution of this disruption in 30-second increments. Results were validated with more traditional endpoint characterization methods including immunofluorescence staining of junctional proteins, permeability assays, and electrical impedance spectroscopy (data not shown). The sensitivity of the OECT sensor is equal to or greater than these established characterization techniques, and benefits from an extremely high temporal resolution. Moreover, the simple fabrication and device operation open up possibilities for creative solutions for large-scale diagnostics screening and *in vitro* model development.



Conclusions

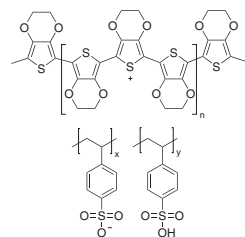
In this article, we discussed two examples of novel organic bioelectronics devices: electrocorticography arrays and organic electrochemical transistors. Electrocorticography arrays designed with PEDOT:PSS electrodes outperform gold electrodes of similar geometry. These PEDOT:PSS based arrays provide a means of recording ECoG signals inside sulci in the human brain, significantly enhancing diagnostic capabilities, primarily due to their unique conformability. Organic electrochemical transistors deliver real-time information on subtle changes in barrier tissue integrity. The information obtained from this device can be used to understand the effect of pathogens and toxins, and the transport of drugs.

References

- (1) Malliaras, G. Organic Bioelectronics: A new era in organic electronics. *Biochem. Biophys. Acta* **2012**.
- (2) Owens, R. M. & Malliaras, G. G. Organic electronics at the interface with biology. *Mrs Bull.* **2010**, *35*, 449-456.
- (3) Berggren, M. & Richter-Dahlfors, A. Organic bioelectronics. *Advanced Materials*, **2007**, *19*, 3201-3213.
- (4) Ludwig, K. A., Uram, J. D., Yang, J. Y., Martin, D. C. & Kipke, D. R. Chronic neural recordings using silicon microelectrode arrays electrochemically deposited with a poly(3,4-ethylenedioxythiophene) (PEDOT) film. *Journal of Neural Engineering*, **2006**, *3*, 59-70.
- (5) Kuruwilla, A. & Flink, R. Intraoperative electrocorticography in epilepsy surgery: useful or not? *Seizure*, **2003**, *12*, 577-584.
- (6) Schalk, G., McFarland, D. J., Hinterberger, T., Birbaumer, N. & Wolpaw, J. R. BCI2000: A general-purpose, brain-computer interface (BCI) system. *IEEE Transactions on Biomedical Engineering*, **2004**, *51*, 1034-1043.
- (7) Kim, D. H. *et al.* Dissolvable films of silk fibroin for ultrathin conformal bio-integrated electronics. *Nature Materials*, **2010**, *9*, 511-517.
- (8) Khodagholy, D. *et al.* Highly Conformable Conducting Polymer Electrodes for In Vivo Recordings. *Advanced Materials*, **2011**, *23*, H268-H272.
- (9) Chagnac-Amitai, Y. & Connors, B. W. Horizontal spread of synchronized activity in neocortex and its control by GABA-mediated inhibition. *J Neurophysiol*, **1989**, *61*, 747-758.
- (10) Jimison, L. H. *et al.* Measurement of Barrier Tissue Integrity with an Organic Electrochemical Transistor. *Advanced Materials*, **2012**, *24*, 5919-5923.
- (11) Farquhar, M. G. & Palade, G. E. Junctional Complexes in Various Epithelia. *The Journal of Cell Biology*, **1963**, *17*, 375-412.
- (12) Artursson, P., Palm, K. & Luthman, K. Caco-2 monolayers in experimental and theoretical predictions of drug transport. *Adv Drug Deliver Rev*, **2001**, *46*, 27-43.
- (13) Bernards, D. A. & Malliaras, G. G. Steady-state and transient behavior of organic electrochemical transistors. *Advanced Functional Materials*, **2007**, *17*, 3538-3544.
- (14) Ivanov, A. I., Nusrat, A. & Parkos, C. A. Endocytosis of Epithelial Apical Junctional Proteins by a Clathrin-mediated Pathway into a Unique Storage Compartment. *Mol Biol Cell*, **2004**, *15*, 176-188.
- (15) Knipp, G. T., Ho, N. F. H., Barsuhn, C. L. & Borchardt, R. T. Paracellular diffusion in Caco-2 cell monolayers: Effect of perturbation on the transport of hydrophilic compounds that vary in charge and size. *Journal of Pharmaceutical Sciences*, **1997**, *86*, 1105-1110.

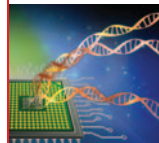
PEDOT Materials

PEDOT:PSS



For a complete list of available materials, visit aldrich.com/polythio.

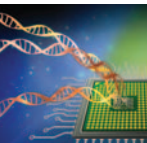
Description	Sheet Resistance (Ω/sq)	Viscosity (cP)	pH	Prod. No.
pellets (dry re-dispersible)	200-450	-	-	768618-1G 768618-5G
1.0 wt. % in H ₂ O, high-conductivity grade	50-120	7-12 at 22 °C	1.8 - 2.2	768642-25G
5.0 wt. % in H ₂ O, conductive grade	50-150	100,000-120,000 at 22 °C	1.5 - 2.0	768650-25G
0.8% in H ₂ O, conductive inkjet ink	75-120 (>80% visible light transmission, 40 μm wet)	7-12 at 22 °C	1.5 - 2.5	739316-25G
1.1% in H ₂ O, neutral pH, high-conductivity grade	<100 (>70% visible light transmission, 40 μm wet)	<100 at 22 °C	5 - 7	739324-100G
1.1% in H ₂ O, surfactant-free, high-conductivity grade	<100 (<80% visible light transmission, 40 μm wet)	<100 at 22 °C	<2.5	739332-100G
0.54% in H ₂ O, high-conductivity grade	<200 (>90% visible light transmission, 40 μm wet)	<18 at 22 °C	<2.7	739340-25G 739340-100G
3.0-4.0% in H ₂ O, high-conductivity grade	500 (4 point probe measurement of dried coating based on initial 18 μm wet thickness.) 1500 (4 point probe measurement of dried coating based on initial 6 μm wet thickness.)	10-30 at 20 °C	1.5 - 2.5 at 25 °C (dried coatings)	655201-5G 655201-25G
2.8 wt % dispersion in H ₂ O, low-conductivity grade	-	<20 at 20 °C	1.2 - 1.8	560596-25G 560596-100G



Other PEDOTs

For a complete list of available materials, visit aldrich.com/polythio.

Name	Structure	Description	Conductivity	Prod. No.
Poly(3,4-ethylenedioxythiophene)		in H ₂ O, dodecylbenzene sulfonic acid (DBSA) as dopant	-	675288-25ML
Poly(3,4-ethylenedioxythiophene), tetramethacrylate end-capped		0.5 wt. % (dispersion in propylene carbonate), <i>p</i> -toluenesulfonate as dopant	0.1-0.5 S/cm (bulk)	649813-25G
Poly(3,4-ethylenedioxythiophene), tetramethacrylate end-capped		0.5 wt. % (dispersion in nitromethane), <i>p</i> -toluenesulfonate as dopant	0.1-0.5 S/cm (bulk)	649821-25G
Poly(3,4-ethylenedioxythiophene), bis-poly(ethyleneglycol), lauryl terminated		0.6-1.1 wt. % 0.8 wt. % (dispersion in propylene carbonate), perchlorate as dopant	10-45 S/cm (bulk)	736287-25G
Poly(3,4-ethylenedioxythiophene), bis-poly(ethyleneglycol), lauryl terminated		0.6-1.0 wt. % (solid) 0.8 wt. % (dispersion in 1,2-dichlorobenzene), <i>p</i> -toluenesulfonate as dopant	0.01-0.05 S/cm (bulk)	736309-25G
Poly(3,4-ethylenedioxythiophene), bis-poly(ethyleneglycol), lauryl terminated		0.7 wt. % (dispersion in nitromethane) 0.5-0.9 wt. % (solid concentration), <i>p</i> -toluenesulfonate as dopant	10 ⁻² -10 ⁻⁴ S/cm (bulk)	736295-25G
Poly(3,4-ethylenedioxythiophene)- <i>block</i> -poly(ethylene glycol) solution		1 wt. % dispersion in nitromethane, perchlorate as dopant	0.1-5.0 S/cm (bulk)	649805-25G



Polyaniline (PANI)

For a complete list of available materials, visit aldrich.com/pani.

Name	Structure	Conductivity	Prod. No.
Polyaniline (emeraldine salt), composite (20 wt.% polyaniline on carbon black)		30 S/cm (pressed pellet)	530565-5G 530565-25G
Polyaniline (emeraldine salt), composite (30 wt.% polyaniline on nylon)		~ 0.5 S/cm (pressed pellet)	577073-10G
Polyaniline (emeraldine salt) short chain, grafted to lignin, powder		1-2 S/cm (pressed pellet)	561126-10G

Polypyrrole (PPy)

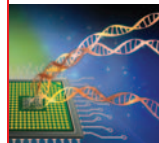
For a complete list of available materials, visit aldrich.com/ppy.

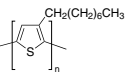
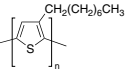
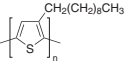
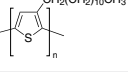
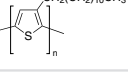
Name	Structure	Description	Conductivity	Prod. No.
Polypyrrole-block-poly (caprolactone)		0.3-0.7 wt. % (dispersion in nitromethane), p-toluenesulfonate as dopant	10-40 S/cm (bulk)	735817-25G
Polypyrrole		composite with carbon black doped, proprietary organic sulfonic acid as dopant	30 S/cm (bulk)	530573-25G
Polypyrrole		proprietary organic sulfonic acid as dopant	10-50 S/cm (pressed pellet)	577030-5G 577030-25G
Polypyrrole		coated on titanium dioxide doped, proprietary organic sulfonic acid as dopant	0.5-1.5 S/cm (pressed pellet, typical)	578177-10G
Polypyrrole		5 wt % dispersion in H ₂ O, doped, proprietary organic acids as dopant	>0.0005 S/cm (dried cast film)	482552-100ML

Polythiophene (PT)

For a complete list of available materials, visit aldrich.com/polythio.

Name	Structure	Regioregularity	Mol. Wt.	Prod. No.
Poly(3-butylthiophene-2,5-diyl), P3BT		regioregular	M _w 54,000 (typical)	495336-1G
Poly(3-butylthiophene-2,5-diyl), P3BT		regiorandom	-	511420-1G
Poly(3-hexylthiophene-2,5-diyl), P3HT, Plexcore® OS 2100		regioregular	M _n 54,000-75,000	698997-250MG 698997-1G 698997-5G
Poly(3-hexylthiophene-2,5-diyl), P3HT, Plexcore® OS 1100		regioregular	M _n 15,000-45,000	698989-250MG 698989-1G 698989-5G
Poly(3-hexylthiophene-2,5-diyl), P3HT		regioregular	-	445703-1G
Poly(3-hexylthiophene-2,5-diyl), P3HT		regiorandom	-	510823-1G



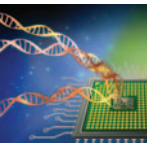
Name	Structure	Regioregularity	Mol. Wt.	Prod. No.
Poly(3-octylthiophene-2,5-diyl), P3OT		regioregular	$M_n \sim 34,000$	445711-1G
Poly(3-octylthiophene-2,5-diyl), P3OT		regioregular	$M_n \sim 25,000$	682799-250MG
Poly(3-decylthiophene-2,5-diyl), P3DT; P3DT-RR		regioregular	$M_n \sim 30,000$ $M_w \sim 42,000$	495344-1G
Poly(3-dodecylthiophene-2,5-diyl), P3DDT		regioregular	$M_w \sim 60,000$	450650-1G
Poly(3-dodecylthiophene-2,5-diyl), P3DDT		regioregular	$M_w \sim 27,000$	682780-250MG

Popular Cell Culture Lines

Sigma Life Science has formed a working partnership with The European Collection of Cell Cultures (ECACC), a world leader and recognized expert in the maintenance, cultivation and distribution of authenticated cell lines. Together, we offer the most diverse selection of cell culture products and services available.

For the complete list of over 1,500 cell lines available worldwide, visit sigma.com/ecacc.

Name	Source	Growth Mode	Morphology	Prod. No.
C2C12 Cell Line from mouse, C3H muscle myoblast	muscle mouse	Adherent	Myoblast	91031101-1VL
MRC-5 PD 19 Cell Line human	lung human	Adherent	Fibroblast-like	05072101-1VL
Hep G2 Cell Line human, hepatocyte carcinoma	liver human	Adherent	Epithelia	85011430-1VL
CACO-2 Cell Line human, Caucasian colon adenocarcinoma	colon human	Adherent	Epithelial	86010202-1VL
MCF7 Cell Line human, breast adenocarcinoma	breast human	Adherent	Epithelial-like	86012803-1VL
THP 1 Cell Line human, Leukemic monocyte	blood human	Suspension	Monocyte	88081201-1VL
RAW 264.7 Cell Line murine, Macrophage from blood	blood mouse	Semi-adherent	Macrophage	91062702-1VL
A2780cis Cell Line human, ovarian carcinoma	ovary human	Adherent	Epithelial	93112517-1VL
A2780 Cell Line human, ovarian carcinoma	ovary human	Adherent	Epithelial	93112519-1VL
SH-SY5Y Cell Line human, Neuroblast from neural tissue.	neural human	Adherent	Neuroblast	94030304-1VL



Flexible Organic Transistors for Biomedical Applications



Tsuyoshi Sekitani,* Kazunori Kuribara, Tomoyuki Yokota, Takao Someya
Department of Electric and Electronic Engineering, Department of Applied Physics,
School of Engineering
University of Tokyo, 7-3-1 Hongo, Bunkyo-ku, Tokyo 113-8656, Japan
Exploratory Research for Advanced Technology (ERATO)
Japan Science and Technology Agency (JST), Tokyo, Japan
*Email: sekitani@ee.t.u-tokyo.ac.jp

Introduction

There is widespread demand for thin, lightweight, and flexible electronic devices such as displays, sensors, actuators, and radio-frequency identification tags (RFIDs). Flexibility is necessary for scalability, portability, and mechanical robustness. Various types of flexible thin-film transistors (TFTs)¹⁻⁵ have been employed to realize flexible electronic devices on plastic substrates, such as solar cells,⁶ light-emitting diodes (LEDs),⁷ TFTs,⁸ memory devices,⁹⁻¹³ sensors,¹⁴ actuators,¹⁵ displays,¹⁶ and transponders.¹⁷ Therefore, mechanical flexibility of flexible electronics has been the focus of intensive research efforts in order to improve mechanical durability and obtain better fundamental understanding of electronic performance under bending stresses.

Recently, flexible electronics have seen widespread use in biomedical applications.¹⁸⁻²² The mechanical flexibility offered by organic circuits has been investigated to develop novel biomedical devices such as large-area sensitive catheters.⁵ To be integrated into medical devices, these organic electronic devices must be able to withstand sterilization conditions (involving exposure to temperatures exceeding 100 °C) in order to achieve asepsis and prevent infection. At such high temperatures organic devices generally degrade, either as a result of thermally induced oxidation of the organic semiconductor, changes in the crystal structure or morphology of thin films, or mechanical stresses induced by mismatches in the thermal expansion of the material stack within the devices. The use of organic electronic devices in biomedical applications will necessarily require a critical understanding and improvement of their thermal stability.

Herein, we demonstrate the fabrication of *heat-resistant, flexible, and high-mobility* organic TFTs and circuits that operate at voltages of 2 V and exhibit a field-effect mobility of 1.2 cm²/Vs. The effects of exposing these TFTs to various temperatures were systematically investigated and it was found that heat-induced changes in the electrical performance of the TFTs were negligible up to 120 °C. Heat-resistant TFTs were achieved using DNIT (dinaphtho-[2,3-b:2',3'-f]-thieno-[3,2-b]-thiophene) (Aldrich Product No. 767638) as an organic semiconductor²³ and a combination of a plasma-grown aluminum oxide (AlO_x) layer and an alkylphosphonic acid self-assembled monolayer (SAM) as a gate dielectric.²⁴ The effects of temperature on the crystal structure of the DNIT film and on the orientation of the alkylphosphonic molecules within the SAM were investigated using X-ray diffraction (XRD) and near edge X-ray absorption fine structure (NEXAFS) spectroscopy, respectively. The practical applicability of heat-resistant organic TFTs was demonstrated by subjecting them to standard medical sterilization procedures, including heating to 150 °C for 20 seconds or 121 °C for 20 minutes in air.²⁵ Similarly, an electronic application, requiring operation of

high-performance and heat-resistant circuits folded with an extremely small bending radius, was simulated using a very thin medical catheter that measures spatial distribution of pressure by wrapping a foldable transistor and sensor matrix around its surface in a helical structure.

Device Fabrication

Organic transistor circuits on a plastic substrate, which exhibit excellent electrical characteristics even at high temperatures, are shown in Figures 1A and 1B. Figure 1C shows a schematic of the heat-resistant TFTs fabricated using a thin AlO_x/SAM gate dielectric on a flexible polyimide substrate. Chemical structures and physical appearance of DNIT (Aldrich Product No. 767638) and alkylphosphonic acid SAMs, *n*-octadecylphosphonic acid (C18-SAM) (Aldrich Product No. 715166) and *n*-tetradecylphosphonic acid (C14-SAM) (Aldrich Product No. 736414), are shown in Figures 1D and 1E, respectively. TFTs were fabricated by depositing a 25-nm thick aluminum layer as the gate electrode onto a 75-μm thick polyimide substrate by thermal evaporation through a shadow mask. Oxygen-plasma treatment with a plasma power of 100 W for 10 minutes was performed to oxidize the surface of the thermally evaporated aluminum, resulting in a thin AlO_x layer on the gate electrode. The substrates were subsequently dipped into 5-mM solution of C18-SAM or C14-SAM in isopropyl alcohol for 16 hours to form a SAM with ~2-nm thickness.²⁴ The combination of AlO_x and SAM functions as the high-insulating gate dielectric layer. A 30-nm thick DNIT layer was then deposited by thermal evaporation to form the channel, followed by a 50-nm thick Au layer through a shadow mask to define the source/drain contacts. Finally, the entire surface of the device was encapsulated with organic/metal hybrid coatings.²⁶

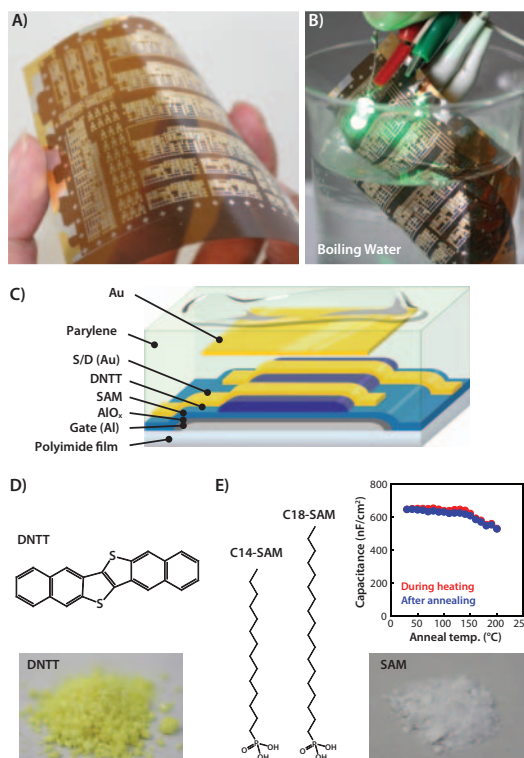
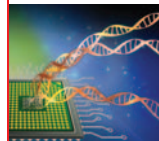


Figure 1. Dinaphtho-[2,3-b:2',3'-f]-thieno-[3,2-b]-thiophene (DNIT) transistors and circuit. **A)** Photograph of heat-resistant, flexible, and high-mobility organic transistor circuit on a plastic substrate. **B)** Photograph of an organic circuit that can operate in boiling water. **C)** Schematic cross section of transistors encapsulated with parylene/Au. **D)** Chemical structures and photographs of the organic semiconductor DNIT. **E)** Chemical structures



and photographs of the alkylphosphonic acid molecules—*n*-octadecylphosphonic acid and *n*-tetradecylphosphonic acid—employed for the SAMs. Capacitance of SAM capacitor consisting of 20-nm Al/4-nm AlO_x/2-nm SAM/50-nm Au is shown as a function of temperature (red line: capacitance measured at annealing temperatures, blue line: measured at room temperature after cooling from annealing temperatures). Adapted from Reference 20.

Thermal Stability and Electrical Properties

The output and transfer characteristics of the DNNT TFT, measured at 30 °C prior to annealing, are shown in **Figures 2A** and **2B**. The typical mobility is 1.2 cm²/Vs and the on/off ratio exceeds 10⁵ at -2 V operation, indicating excellent TFT characteristics. Performance did not change even after encapsulation (**Figure 2B**). The effects of annealing were systematically evaluated by comparing the electrical characteristics of the TFTs at 30 °C to the characteristics after annealing at 40 °C for 30 minutes. The devices were then allowed to cool to 30 °C and the characteristics were measured again. The same transistors were then annealed at 50 °C for 30 minutes, cooled to 30 °C, and measured again. This procedure was performed from 30 to 160 °C in temperature increments of 10 °C. All of these experiments were carried out in a nitrogen-filled glove box with less than 1 ppm of oxygen and moisture. **Figure 2C** shows the transfer characteristics with varying annealing temperatures as measured at room temperature. The on-state drain current (*I*_{DS}) at gate-source voltage (*V*_{GS}) = drain-source voltage (*V*_{DS}) = -2 V decreases slightly upon annealing at 100 °C due to a shift in the threshold voltage toward more negative values. As shown in **Figure 2D**, the thermal stability of the DNNT TFT with parylene encapsulation is higher than without encapsulation, which is mainly due to high thermal stability of the parylene used. Further annealing above 150 °C results in a degradation of the electrical performance.

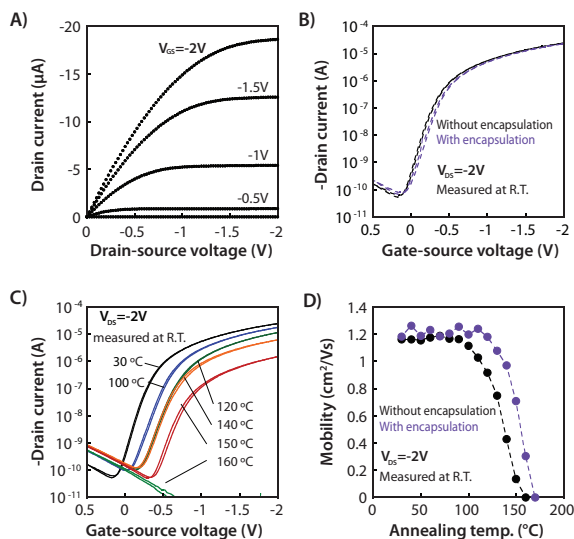


Figure 2. Electrical properties of DNNT transistors. **A)** Output curves of a DNNT TFT before annealing, and **B)** gate-source voltages (*V*_{GS}) applied with change from 0 to -2 V in steps of -0.5 V. DC characteristics of a DNNT TFT are measured at room temperature before and after encapsulation. **C)** DC characteristics of a DNNT TFT measured at room temperature before and after various thermal processes. Transfer curves of a DNNT TFT after annealing in a nitrogen-filled glove box with less than 1 ppm oxygen and moisture at different temperatures. A drain-source voltage (*V*_{DS}) of -2 V was applied. For each measurement, the TFT was annealed at the indicated temperature and then allowed to cool to 30 °C for the measurement. Annealing temperatures were changed from 40 to 170 °C. **D)** Mobility as a function of annealing temperature where transistors with and without encapsulation are compared. Measurements are performed in nitrogen gas. Adapted from Reference 20.

The effects of annealing at elevated temperatures on the structure of the DNNT films were evaluated by XRD measurements using Cu-Kα X-ray radiation ($\lambda = 1.541 \text{ \AA}$).²⁵ The in-plane XRD spectrum of DNNT show three diffraction peaks. A comparison with the X-ray crystallography of single-crystal DNNT^{23,27} indicates these three unique peaks correspond to the (110), (020), and (120) lattice planes of DNNT. The diffraction peaks at $2\theta = 23^\circ$ and 27° were found to shift slightly toward larger diffraction angles upon annealing above 100 °C, which corresponds to the temperature beyond which the electrical degradation of the DNNT TFTs begins. From the observed shift of the diffraction peaks, the change of the lattice constants upon annealing can be estimated. In particular, the lattice constant along the *a*-axis increases by 1.5% from 6.10 to 6.19 Å upon annealing at 160 °C. On the other hand, the lattice constant along the *b*-axis decreases only slightly by 0.65% from 7.77 to 7.72 Å; whereas, the lattice spacing along the *c*-axis decreases negligibly by 0.3% from 16.36 to 16.31 Å upon annealing at 160 °C. The observed reduction in the field-effect mobility (from 1.2 to 0.4 cm²/Vs after annealing at 140 °C) is thus attributed to changes induced in the crystal structure of the DNNT film by the following two mechanisms: 1) a phase transition induced at 100 °C that reduces the conductivity within the grains; and 2) a change in the grain shape that reduces the contacts between neighboring grains. The latter mechanism was evidenced from atomic force microscopy (AFM) observations of the DNNT morphology, which revealed that after annealing at 140 °C, the film roughens significantly and features as high as 300 nm begin to emerge.

The thermal stability and electrical performance of gate dielectrics comprising a thin plasma-grown AlO_x layer and an alkylphosphonic acid SAM were evaluated from measurements on capacitors consisting of a 20-nm thick Al bottom electrode, a 4-nm thick AlO_x layer, a 2-nm thick SAM, and a 50-nm thick Au top electrode. The capacitance of the AlO_x/SAM dielectric is stable up to 150 °C; however, it decreases slightly upon annealing at 160 °C (**Figure 1E**).

The molecular orientation and stability of the SAM at elevated temperatures were examined using NEXAFS spectroscopy.^{25,28-30} The integrated intensity of the first angle-dependent s*_{C-H} resonance is evaluated as a function of the X-ray incident angle. The analysis yielded a dichroic ratio (DR) value of 0.5-0.6 for the SAM, suggesting the alkylphosphonic acid molecules within the SAM are oriented with their chains preferentially upright with respect to the substrate; this degree of preferential orientation indicated by the DR is among the highest reported for SAMs. This preferential orientation of the alkylphosphonic acid molecules is maintained up to a temperature of 200 °C, confirming the excellent thermal stability of the SAMs. Analysis with the Building Block Model indicates the molecules within the SAM are tilted with an angle of 13-18° from the surface normal (**Figure 3**), and this tilt angle is largely preserved upon thermal annealing at elevated temperatures.

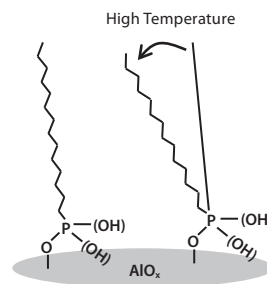
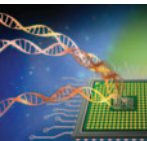


Figure 3. Schematic illustration of SAM. The tilt angle of SAM is increased at high temperatures.



Medical Sterilization Procedures on Organic Transistors

Medical sterilization typically involves thermal processes, e.g., heating in an autoclave at 121 °C for 20 minutes with moisture at a pressure of 2 atm or at 150 °C for 20 seconds with moisture at a pressure of 1 atm. The practical applicability of our heat-resistant flexible organic transistors for medical instruments and their ability to simultaneously offer high thermal stability, mechanical flexibility, and sustained electrical performance were demonstrated by subjecting the TFTs to typical sterilization treatments up to 150 °C. We also carried out sterilization at 121 °C for 20 minutes under atmospheric pressure.

The temperature suitability for sterilization was assessed using yeast cells stained with two different dyes: DAPI salt (4',6-diamidino-2-phenylindole dihydrochloride, [Sigma Product No. D9542](#)), which stains all yeast cells and shows blue fluorescence when excited with UV light; and propidium iodide ([Sigma Product No. P4170](#)), which preferentially stains dead cells and shows red fluorescence when excited with green light. After sterilization at 150 °C for 20 seconds or at 121 °C for 20 minutes in air, the quantification of the fluorescence intensities indicated that 93% of the yeast cells were killed upon sterilization. On the other hand, the on-state drain current (more than 1 μA) and the on/off ratio (8×10^5) remained practically unaffected by these sterilization procedures.

Flexible Organic Circuits for Medical Catheter

By exploiting the low-temperature processes of the air-stable, heat-resistant, organic semiconducting layer and the SAM gate dielectric layer, various substrates can be used for the fabrication of organic transistors, such as rubber,^{31, 32} conventional polyethylene naphthalate (PEN) with low- T_g ,³³ and very thin plastic substrates.⁵

For an electronic application that requires the operation of high-performance circuits folded with an extremely small bending radius, we demonstrated the implementation of organic integrated circuits (ICs) on the inner and outer surfaces of ultrafine rubber tubes with a diameter of 1 mm.⁵ Due to its novel helical structure and great flexibility, the electrically functionalized tube can bend around turns or corners, and hence, be wrapped around objects. To demonstrate a possible application for organic TFTs operating in the bent state, we manufactured a thin catheter to measure the spatial distribution of mechanical pressure. The sensor was fabricated by laminating three sheets (**Figure 4**): a foldable 4x36 array of pentacene ([Aldrich Product No. 698423](#)) TFTs, a pressure-sensitive rubber sheet, and a 12.5- μm thick polyimide sheet with a gold counter electrode. The source contacts of all 144 transistors were connected to the rubber sheet; whereas, the counter electrode was in contact with the opposite surface of the rubber sheet. Upon application of mechanical pressure to the catheter, the electrical resistance between the top and the bottom surfaces of the rubber sheet decreased. A potential of -3 V applied to the counter electrode was supplied to the TFTs at those positions where pressure was applied; thus, the spatial distribution of pressure was obtained by probing the TFTs in the active-matrix array. We believe this approach will lead to various new applications ranging from the functionalization of catheters to artificial blood tubes with pressure sensors. To show the feasibility of the new concept, we also demonstrated the measurement of mechanical pressure using organic transistor-based pressure sensors in this configuration.

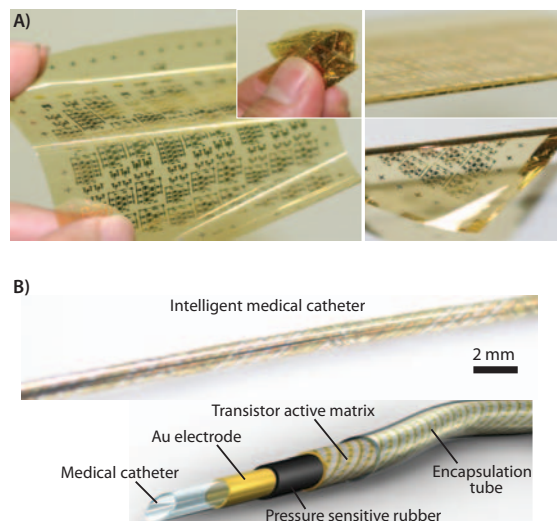


Figure 4. Heat-resistant flexible circuit for applications to biomedical electronic devices. **A)** 12.5- μm -thick polyimide substrate with functional organic TFTs and organic complementary circuits. The array has an area of $75 \times 75 \text{ mm}^2$. **B)** A transistor active-matrix array in the shape of a tightly wound helix. An ultraflexible active-matrix pressure sensor array as a concept of a catheter that measures the spatial distribution of pressure along its length and circumference by means of an active-matrix sensor helix. Adapted from Reference 5.

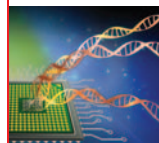
Conclusions and Future Prospects

Heat-resistant, flexible, organic thin-film transistors have been demonstrated to withstand the harsh conditions of medical sterilization procedures. One of the most attractive features of flexible electronics is their biocompatibility. In addition to wearable electronics including sensors and actuators that operate outside the body, implantable electronics that function inside the body are expected to play important roles in healthcare. For example, flexible pressure and thermal sensors can realize electrically powered artificial skin, and flexible vibration and photodetectors can work as an electrically powered artificial *auris interna* and retina, respectively. Given their excellent mechanical flexibility and softness, users might implant those with the lower resistance to electronic objects in the body. Furthermore, if the flexible organic circuits are comprised of biocompatible materials, electronic implants can be used inside the body without fear of immune rejection.

Apart from their applications in healthcare, flexible electronics should find applications in electronic devices that are used in daily life. For example, flexible organic circuits fabricated on banknotes can be used as an ultimate anticounterfeit technology and tracking system. Organic ICs with exceptional flexibility and bending stability can realize new concepts in electronics and open up human-friendly electronic systems.

Acknowledgments

This study was partially supported by KAKENHI (Wakate S & Wakate A), and the Special Coordination Funds for Promoting and Technology. We thank Dr. He Wang, Prof. Yueh-Lin Loo (Princeton University), Dr. Chernob Jaye, Dr. Daniel Fischer (National Institute of Standards and Technology) for the NEXAFS measurements and discussion; Dr. Hagen Klauk, Dr. Ute Zschieschang (Max Planck Institute for Solid State Research) for the SAM technology; and Dr. Tatsuya Yamamoto, Prof. Kazuo Takimiya (Hiroshima University), Dr. Masaaki Ikeda, Hirokazu Kuwabara (Nippon Kayaku Co., Ltd.) for DNNT, Prof. Takayasu Sakurai, and Prof. Makoto Takamiya (University of Tokyo) for the circuit design. We also thank Dojindo Molecular Technologies Inc. for the high-purity fluorescent dye and Daisankasei Co., Ltd., for the high-purity parylene (diX-SR).



References

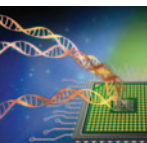
- (1) Kodaira, T. et al. *J. SID* **2008** 16/1, 107-111.
- (2) Nomura, K., Ohta, H., Takagi, A., Kamiya, T., Hirano, M., and Hosono, H. *Nature* **2004** 432, 488-492.
- (3) Gleskova, H., Wagner, S., Soboyejo, W., and Suo, Z. *J. Appl. Phys.* **2002** 92, 6224.
- (4) Sekitani, T. et al. *Appl. Phys. Lett.* **2005** 87, 173502.
- (5) Sekitani, T., Zschieschang, U., Klauk, H., and Someya, T., *Nature Mater.* **2010** 9, 1015.
- (6) Kaltenbrunner, M. et al., *Nature Commun.* **2012** 3, 770.
- (7) Müller, C. D. et al. *Nature* **2003** 421, 829-833.
- (8) Gelinck, G. H. et al. *Nature Mater.* **2004** 3, 106-110.
- (9) Möller, S., Perlov, C., Jackson, W., Taussig, C., and Forrest, S. R. *Nature* **2003** 426, 166-169.
- (10) Ouyang, J., Chu, C.-W., Szmanda, C. R., Ma, L., and Yang, Y. *Nature Mater.* **2004** 3, 918-922.
- (11) Naber, R. C. G. et al. *Nature Mater.* **2005** 4, 243-248.
- (12) Asadi, K. de Leeuw, D. M., de Boer, B., and Blom, P. *Nature Mater.* **2008** 7, 547-550.
- (13) Sekitani, T. et al. *IEEE Trans. Electr. Dev.* **2009** 56, 1027-1035.
- (14) Someya, T. et al. *Proc. Natl. Acad. Sci. U.S.A.* **2005** 102, 12321-12325.
- (15) Sekitani, T. et al. *Nature Mater.* **2007** 6, 413-417.
- (16) Zhou, L. et al. *Appl. Phys. Lett.* **2006** 88, 083502.
- (17) Baude, P. et al. *Appl. Phys. Lett.* **2003** 82, 3964-3966.
- (18) Kim, D. H. et al. *Science* **2008** 320, 507-511.
- (19) Viventi, J. et al. *Nat. Neurosci.* **2011** 14, 1599.
- (20) Qing, Q. et al. *Proc. Natl. Acad. Sci. USA* **2010** 107, 1882-1887.
- (21) Mannsfeld, S. C. B. et al. *Nat. Mater.* **2010** 9, 859.
- (22) Berggren, M., Dahlfors, A. R. *Adv. Mater.* **2007** 19, 3201
- (23) Yamamoto T. and Takimiya, K. *J. Am. Chem. Soc.* **2007** 129, 2224-2225.
- (24) Klauk, H., Zschieschang, U., Pflaum, J., and Halik, M. *Nature* **2007** 445, 7129 745-748.
- (25) Kuribara, K. et al. *Nature Comm.* **2012** 3, 723.
- (26) Sekitani, T. and Someya, T. *Jpn. J. Appl. Phys.* **2007** 46, 4300.
- (27) Yamamoto, T., Shinamura, S., Miyazaki, E., and Takimiya, K., *Bull. Chem. Soc. Jpn.* **2010** 83, 120-130.
- (28) DelRio, F. W., Jaye, C., Fischer, D. A., and Cook, R. F. *Appl. Phys. Lett.* **2009** 94, 131909.
- (29) Krapchetov, D. A., Ma, H., Jen, A. K. Y., Fischer, D. A., and Loo, Y.-L. *Langmuir* **2008** 24, 851-856.
- (30) Lee, K. S., Smith, T. J., Dickey, K. C., Yoo, J. E., Stevenson, K. J., and Loo, Y.-L., *Adv. Funct. Mater.* **2006** 16, 2409-2414.
- (31) Sekitani, T. et al. *Nature Mater.* **2009** 8, 494.
- (32) Sekitani, T. et al. *Science* **2008** 321, 1468.
- (33) Sekitani, T. et al. *Science* **2009** 326, 1516.

Organic Semiconductors

P-type Small Molecules

For a complete list of available materials, visit aldrich.com/psmall.

Name	Structure	Purity	Mobility	Prod. No.
Benz[<i>b</i>]anthracene, Tetracene; 2,3-Benzanthracene; Naphthacene		99.99% trace metals basis, sublimed grade	0.4 cm ² /Vs	698415-1G
Benz[<i>b</i>]anthracene, Tetracene; 2,3-Benzanthracene; Naphthacene		98%	0.4 cm ² /Vs	B2403-100MG B2403-500MG B2403-1G
Pentacene		≥99.995% trace metals basis, triple-sublimed grade	0.4-3 cm ² /Vs	698423-500MG
Pentacene		≥99.9% trace metals basis, sublimed grade	0.4-3 cm ² /Vs	684848-1G
Pentacene		99%	0.4-3 cm ² /Vs	P1802-100MG P1802-1G P1802-5G
6,13-Diphenylpentacene		98%	8×10 ⁻⁵ cm ² /Vs	760641-1G
6,13-Bis(triethylsilyl)ethynyl)pentacene, TES pentacene		≥99%, HPLC	10 ⁻⁵ cm ² /Vs	739278-100MG 739278-500MG
5,5'-Dihexyl-2,2'-bithiophene, DH-2T		96%	-	632953-1G
5,5'-Di(4-biphenyl)-2,2'-bithiophene, 5,5'-[Di(1,1'-biphenyl)-4-yl]-2,2'-bithiophene		97%	0.04 cm ² /Vs	695947-1G
FTTF, 5,5'-Di(9 <i>H</i> -fluoren-2-yl)-2,2'-bithiophene		sublimed grade	0.3 cm ² /Vs	754056-250MG
DH-FTTF, 5,5'-Bis(7-hexyl-9 <i>H</i> -fluoren-2-yl)-2,2'- bithiophene		95%	0.05-0.12 cm ² /Vs	754064-250MG
2,2':5',2'':5''-Quaterthiophene, α-Quarterthienyl; 4T		96%	1.2×10 ⁻³ cm ² /Vs	547905-1G
α-Sexithiophene, 6T; Sexithiophene		-	0.075 cm ² /Vs	594687-1G



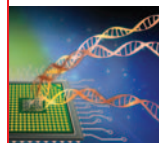
Name	Structure	Purity	Mobility	Prod. No.
5,5''''-Dihexyl-2,2',5',2'',5'',2''',5''',2''''-sexithiophene, DH-6T; α,ω -Dihexylsexithiophene		-	0.13 cm ² /Vs	633216-500MG
Dinaphtho[2,3-b:2',3'-f]thieno[3,2-b]thiophene, DNNT; Naphtho[2,3-b]naphtho[2',3':4,5]thieno[2,3-d]thiophene		99%, sublimed grade	2 cm ² /Vs	767638-100MG 767638-500MG
2,7-Diphenyl[1]benzothieno[3,2-b][1]benzothiophene, DPh-BTBT; 2,7-Diphenylbenzo[<i>b</i>]benzo[4,5]thieno[2,3- <i>d</i>]thiophene		99%, sublimed grade	2 cm ² /Vs	767603-100MG 767603-500MG
2,6-Diphenylbenzo[1,2- <i>b</i> :4,5- <i>b'</i>]dithiophene, DPh-BDT		97%, sublimed grade	4.6x10 ⁻³ cm ² /Vs	767611-100MG 767611-500MG
2,6-Ditolylbenzo[1,2- <i>b</i> :4,5- <i>b'</i>]dithiophene, DT-BDT		95%, sublimed grade	10 ⁻² cm ² /Vs	767646-100MG 767646-500MG
Naphtho[1,2- <i>b</i> :5,6- <i>b'</i>]dithiophene, NDT		97%	>0.5 cm ² /Vs	768677-500MG
ADT, Anthra[2,3- <i>b</i> :6,7- <i>b'</i>]dithiophene		97%	0.3 cm ² /Vs	754080-250MG
TES-ADT, 5,11-Bis(triethylsilyl)ethynyl)anthradithiophene		>99%, HPLC	1 cm ² /Vs	754102-100MG
diF-TES-ADT, 2,8-Difluoro-5,11-bis(triethylsilyl)ethynyl)anthradithiophene		99%, HPLC	1 cm ² /Vs	754099-100MG
SMDPPEH, 2,5-Di-(2-ethylhexyl)-3,6-bis-(5''- <i>n</i> -hexyl-[2,2',5',2'']terthiophen-5-yl)-pyrrolo[3,4- <i>c</i>]pyrrole-1,4-dione		97%, HPLC	~10 ⁻⁴ cm ² /Vs	753912-250MG
SMDPPO, 2,5-Dioctyl-3,6-bis-(5''- <i>n</i> -hexyl-[2,2',5',2'']terthiophen-5-yl)-pyrrolo[3,4- <i>c</i>]pyrrole-1,4-dione		-	-	753920-250MG

P-type Polymers

See the Polythiophene (PT) table for poly(3-alkylthiophene) (P3AT) p. 6.

For a complete list of available materials, visit aldrich.com/ppoly.

Name	Structure	Mol. Wt.	Mobility	Prod. No.
PBTTT-C14, Poly[2,5-bis(3-tetradecylthiophen-2-yl)thieno[3,2- <i>b</i>]thiophene]		M _w 20,000-80,000	1.3 cm ² /Vs	753971-250MG
PBTTT-C12, Poly[2,5-bis(3-dodecylthiophen-2-yl)thieno[3,2- <i>b</i>]thiophene]		M _w 20,000-80,000	0.2-0.6 cm ² /Vs	753963-250MG

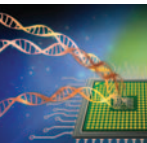


Name	Structure	Mol. Wt.	Mobility	Prod. No.
PCPDtBT, Poly[2,6-(4,4-bis-(2-ethylhexyl)-4H-cyclopenta[2,1-b;3,4-b']dithiophene)-alt-4,7(2,1,3-benzothiadiazole)]		M_w 7,000-20,000	6.8×10^{-3} cm ² /Vs	754005-100MG
PSiF-DBT, Poly[2,7-(9,9-dioctyl-dibenzosilole)-alt-4,7-bis(thiophen-2-yl)benzo-2,1,3-thiadiazole], Poly[2,1,3-benzothiadiazole-4,7-diy-2,5-thiophenediy(9,9-dioctyl-9H-9-silafluorene-2,7-diy)-2,5-thiophenediy]		M_n 10,000-80,000	10^{-3} cm ² /Vs	754021-100MG
PFO-DBT, Poly[2,7-(9,9-dioctylfluorene)-alt-4,7-bis(thiophen-2-yl)benzo-2,1,3-thiadiazole]		M_w 10,000-50,000	3×10^{-4} cm ² /Vs	754013-100MG
PCDTBT, Poly[N-9'-heptadecanyl-2,7-carbazole-alt-5,5-(4',7'-di-2-thienyl-2',1',3'-benzothiadiazole)] ; Poly[[9-(1-octylnonyl)-9H-carbazole-2,7-diy]-2,5-thiophenediy-2,1,3-benzothiadiazole-4,7-diy-2,5-thiophenediy]		M_w 20,000-100,000	6×10^{-5} cm ² /Vs	753998-100MG
Poly[(9,9-dioctylfluorenyl-2,7-diy)-co-bithiophene], Poly(9,9-dioctylfluorene-alt-bithiophene); F8T2; Poly[[2,2'-bithiophene]-5,5'-diy(9,9-dioctyl-9H-fluorene-2,7-diy)]		M_n >20,000	5×10^{-3} cm ² /Vs	685070-250MG
Poly(3-octylthiophene-2,5-diy)-co-3-decyloxythiophene-2,5-diy), POT-co-DOT		M_n 8,000 M_w 21,000	-	696897-250MG

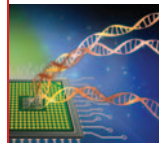
N-type Small Molecules

For a complete list of available materials, visit aldrich.com/nsmall.

Name	Structure	Purity	Mobility	Prod. No.
2,2'-Bis[4-(trifluoromethyl)phenyl]-5,5'-bithiazole		97%	1.83 cm ² /Vs	749257-500MG
5,5'''-Bis(tridecafluorohexyl)-2,2':5',2''':5'',2''-quaterthiophene, DFH-4T; α,ω -Diperfluorohexyl-quaterthiophene		-	≤ 0.64 cm ² /Vs	764639-250MG 764639-1G
1,2,3,4,5,6,7,8-Octafluoro-9,10-bis[4-(trifluoromethyl)phenyl]anthracene		97%	-	757179-1G
1,2,3,4,5,6,7,8-Octafluoro-9,10-bis[2-(2,4,6-trimethylphenyl)ethynyl]anthracene, 1,2,3,4,5,6,7,8-Octafluoro-9,10-bis(mesitylethynyl)anthracene		97%	-	758442-250MG
2,7-Dihexylbenzo[<i>lmn</i>][3,8]phenanthroline-1,3,6,8(2 <i>H</i> ,7 <i>H</i>)-tetrone, NDI-C6; N,N'-(1-Hexyl)-1,4,5,8-naphthalenetetracarboxyldiamide		98%	0.7 cm ² /Vs	768464-500MG
1,3,6,8(2 <i>H</i> ,7 <i>H</i>)-Tetraone, 2,7-dicyclohexylbenzo[<i>lmn</i>][3,8]phenanthroline		98%	6 cm ² /Vs	761443-1G
N,N'-Dimethyl-3,4,9,10-perylene-dicarboximide, MePTC-DI; MePTC; 2,9-Dimethyl-anthra[2,1,9-def:6,5,10-d'e'f']disoquinoline-1,3,8,10(2 <i>H</i> ,9 <i>H</i>)-tetrone		98%	10^{-5} cm ² /Vs	771481-1G 771481-5G



Name	Structure	Purity	Mobility	Prod. No.
2,9-Dipropylanthra[2,1,9- <i>def</i> 6,5,10- <i>d'e'f'</i>]diisoquinoline-1,3,8,10(2 <i>H</i> ,9 <i>H</i>)tetrone, PDI-C3; Bis(<i>n</i> -propylimido)perylene; Perylene-3,4,9,10-tetracarboxylic acid bis(propylimide)		97%	0.1-2.1 cm ² /V/s	771635-1G
<i>N,N'</i> -Dipentyl-3,4,9,10-perylenedicarboximide, PTCDI-C5		98%	0.1 cm ² /V/s	663921-500MG
2,9-Dihexylanthra[2,1,9- <i>def</i> 6,5,10- <i>d'e'f'</i>]diisoquinoline-1,3,8,10(2 <i>H</i> ,9 <i>H</i>)tetrone, PDI-C6; <i>N,N'</i> -Dihexyl-3,4,9,10-perylenedicarboximide		98%	0.1-2.1 cm ² /V/s	773816-1G
2,9-Diheptylanthra[2,1,9- <i>def</i> 6,5,10- <i>d'e'f'</i>]diisoquinoline-1,3,8,10(2 <i>H</i> ,9 <i>H</i>)tetrone, PDI-C7; HepPTC; <i>N,N'</i> -Diheptyl-3,4,9,10-perylenedicarboximide		99%	1.4x10 ⁻² cm ² /V/s	773824-1G
<i>N,N'</i> -Dioctyl-3,4,9,10-perylenedicarboximide, PTCDI-C8		98%	1.7 cm ² /V/s	663913-1G
<i>N,N'</i> -Diphenyl-3,4,9,10-perylenedicarboximide, PTCDI-Ph		98%	10 ⁻⁵ cm ² /V/s	663905-500MG
<i>N,N'</i> -Bis(2,5-di- <i>tert</i> -butylphenyl)-3,4,9,10-perylenedicarboximide		-	1.8x10 ⁻⁴ cm ² /V/s	264229-100MG
2,9-Bis[(4-methoxyphenyl)methyl]anthra[2,1,9- <i>def</i> 6,5,10- <i>d'e'f'</i>]diisoquinoline-1,3,8,10(2 <i>H</i> ,9 <i>H</i>)tetrone, <i>N,N'</i> -Bis(4-methoxybenzyl)perylene-3,4,9,10-bis(dicarboximide)		-	0.5 cm ² /V/s	771627-1G
1,3,8,10(2 <i>H</i> ,9 <i>H</i>)-Tetraone, 2,9-bis(2-phenylethyl)anthra[2,1,9- <i>def</i> 6,5,10- <i>d'e'f'</i>]diisoquinoline, PEPTC		98%, elemental analysis	1.4 cm ² /V/s	761451-1G
2,9-Bis[2-(4-fluorophenyl)ethyl]anthra[2,1,9- <i>def</i> 6,5,10- <i>d'e'f'</i>]diisoquinoline-1,3,8,10(2 <i>H</i> ,9 <i>H</i>)tetrone, 4FPEPTC; <i>N,N'</i> -Bis[2-(4-fluorophenyl)ethyl]-3,4,9,10-perylenetetracarboximide		95%	-	763942-1G
2,9-Bis[2-(4-chlorophenyl)ethyl]anthra[2,1,9- <i>def</i> 6,5,10- <i>d'e'f'</i>]diisoquinoline-1,3,8,10(2 <i>H</i> ,9 <i>H</i>)tetrone, PEPTC; <i>N,N'</i> -Bis[2-(4-chlorophenyl)ethyl]-3,4,9,10-perylenetetracarboximide		-	-	767468-1G
DBP, Dibenzo[[f,f']-4,4',7,7'-tetraphenyl]diindeno[1,2,3-cd:1',2',3'-lm]perylene; 5,10,15,20-Tetraphenylbisbenz[5,6]indeno[1,2,3-cd:1',2',3'-lm]perylene; Red 2		98%, HPLC	-	753939-250MG
4-(1,3-Dimethyl-2,3-dihydro-1 <i>H</i> -benzoimidazol-2-yl)- <i>N,N'</i> -diphenylaniline		98%	-	763721-1G



Name	Structure	Purity	Mobility	Prod. No.
Tin(IV) hexadecafluorophthalocyanine dichloride, Di-chlorotin(IV) hexadecafluorophthalocyanine		-	>0.01 cm ² /Vs	761230-1G
5,10,15,20-Tetrakis(pentafluorophenyl)-21 <i>H</i> ,23 <i>H</i> -porphine palladium(II), Pd(II) meso-tetra(pentafluorophenyl)porphine		-	-	673587-100MG

N-type Polymers

For a complete list of available materials, visit aldrich.com/npoly.

Name	Structure	Mobility	Prod. No.
Poly(benzimidazobenzophenanthroline), BBL		0.1 cm ² /Vs 0.4 cm ² /Vs	667846-250MG 667846-1G
Poly(5-(3,7-dimethyloctyloxy)-2-methoxy-cyanoterephthalylidene)		~10 ⁻⁵ cm ² /Vs	646628-250MG
Poly(5-(2-ethylhexyloxy)-2-methoxy-cyanoterephthalylidene)		~10 ⁻⁵ cm ² /Vs	646644-250MG
Poly(2,5-di(hexyloxy)cyanoterephthalylidene)		~10 ⁻⁵ cm ² /Vs	646652-250MG
Poly(2,5-di(3,7-dimethyloctyloxy)cyanoterephthalylidene)		~10 ⁻⁵ cm ² /Vs	646571-250MG



Phosphonic Acids for Self-assembly

For a complete list of available materials, visit aldrich.com/phosphonic.

Name	Structure	Purity	Prod. No.
Benzylphosphonic acid		97%	737887-1G 737887-5G
4-Fluorobenzylphosphonic acid		99%, HPLC	767956-1G
2,3,4,5,6-Pentafluorobenzylphosphonic acid		97%	737917-1G
4-Nitrobenzylphosphonic acid		97%	754439-1G
Butylphosphonic acid		-	737933-1G 737933-5G
Hexylphosphonic acid		95%	750034-1G 750034-5G
Octylphosphonic acid		97%	735914-1G 735914-5G
1H,1H,2H,2H-Perfluorooctanephosphonic acid		95%	737461-1G 737461-5G
Decylphosphonic acid		97%	737925-1G 737925-5G
Tetradecylphosphonic acid		97%	736414-1G 736414-5G
Hexadecylphosphonic acid		97%	736244-1G 736244-5G
Octadecylphosphonic acid		97%	715166-1G
6-Phosphonohexanoic acid		97%	693839-1G
11-Phosphonoundecanoic acid		96%	678031-1G
16-Phosphonohexadecanoic acid		97%	685801-1G
1,8-Octanediphosphonic acid		97%	699888-1G
1,10-Decyldiphosphonic acid		>97%	737410-1G
(12-Phosphonododecyl)phosphonic acid		97%	685437-1G

Plexcore[®] Organic Conductive Inks and Ink Kits

Freedom to Tune Your Hole Injection Layers (HILs)

Plexcore[®] organic conductive inks with varying resistivities and work functions enable highly tunable HILs.

Inks selection now available as kits or individually!

Name	Resistivity ($\Omega \cdot \text{cm}$)	Work Function (eV)	Aldrich Prod. No.
Plexcore [®] OC RG-1100	25 • 250	5.1–5.2	699799
Plexcore [®] OC RG-1200	500 • 3000	5.1–5.2	699780
Organic Conductive Inks Kit			719102
Plexcore [®] OC RG-1110	10 • 300	4.8	719110
Plexcore [®] OC RG-1115	10 • 300	5.25	719129
Plexcore [®] OC RG-1150	300 • 1000	4.8	719137
Plexcore [®] OC RG-1155	300 • 1000	5.25	719145

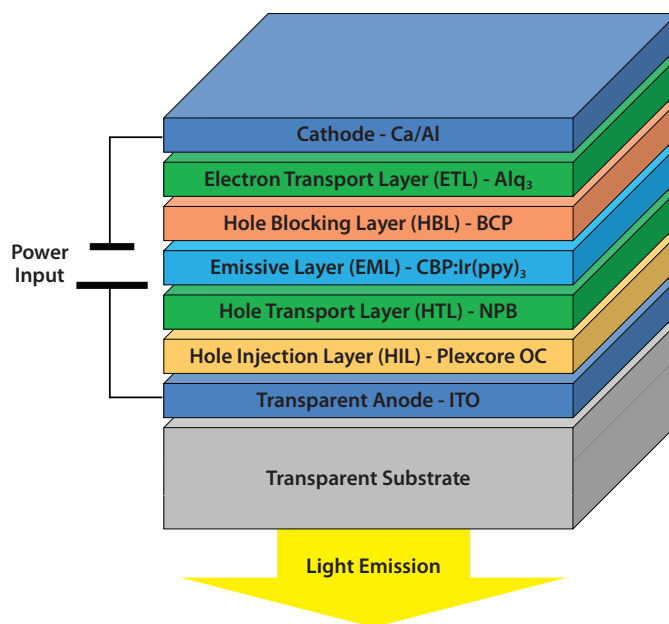
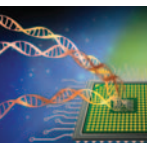


Figure. OLED device cross-sectional structure

For detailed product and application information on the Plexcore[®] conductive inks, view the Tech Spotlight:

aldrich.com/ocinks



Sorting Carbon Nanotubes and Their Biological Applications



Hyunkyu Oh and Sang-Yong Ju*
Department of Chemistry, Yonsei University
Seoul 120-749, Korea
*Correspondence Email: syju@yonsei.ac.kr

Introduction

Carbon nanotubes (CNTs) have received much attention since their discovery in 1991 by Sumio Iijima¹ due to their excellent mechanical, electrical, and optical properties. Like other nanostructures (e.g., quantum dots, nanowires), the physical properties of CNTs are determined by the size and structure of the atoms. CNTs have great potential for applications in transistors, transparent films, infrared emitters, sensors, scanning probes, structural materials, catalysts, etc.^{2,3} Batch-produced CNTs contain a mixture with varying physical properties. Because performance depends on these properties, sorting these tubes by their physical properties (metallicity, chirality, handedness, length, etc.) is critical for cutting-edge applications. Here, we review several methodologies to purify CNTs according to their physical properties and describe related biological applications using the separated CNTs.

Single-walled carbon nanotubes (SWNTs) consist of a seamlessly rolled-up graphene sheet with only sp^2 carbons. SWNTs have physical properties dependent on the direction of the rolling vector (or chiral vector), termed by a pair of integers (n, m). If $n - m$ is a multiple of 3, the tube displays a metallic character; otherwise, it is semiconducting with a bandgap around 1 eV. Semiconducting CNTs have an excitonic bandgap,⁴ which gives rise to photoluminescence (PL).⁵ The PL of CNTs is roughly inversely proportional to their diameter (d_t). CNTs near 1 nm in diameter show PL around 1,200 nm, although the peak positions of PL are strongly dependent on the chirality of the CNT. Commercially available CoMoCAT® (Co-Mo bimetallic catalyst synthesized) tubes⁶ (Aldrich Product Nos. 704113, 724777, 775533 and 773735) show PL in the range of 930-1,450 nm in the near infrared (NIR) regions. This NIR emitting feature is very useful for bioimaging, since the subcutaneous penetration depth of PL in the NIR region is much greater than for visible wavelengths.

Covalent vs. Noncovalent Functionalization

In order to attain biological functionalization of carbon nanotubes, two main methods (covalent and noncovalent functionalization) are generally employed. Covalent functionalization provides intact chemical functionalities on the carbon nanotubes, which can intimately interface with a biologically derived surface (shown in Figures 1A and 1B). However, covalent functionalization disrupts the integrity of the π -conjugated network of sidewalls and ends of carbon nanotubes, which affects their intrinsic properties. The carboxylation of CNTs, as seen in Aldrich Product No. 755125, is the most popular covalent functionalization method and is accomplished by the oxidation of CNTs

via carbodiimide chemistry.⁷⁻⁹ Strong acids (e.g., sulfuric acid and nitric acid) are used for the oxidative functionalization, which breaks the π -conjugated network on nanotubes and functionalizes nanotubes with oxygenated species (i.e., carboxylic acids and phenols).¹⁰ This leaves many defects behind and affects the optical, electrical, and mechanical properties of the CNTs.

Noncovalent functionalization of CNTs (Figures 1C through 1E) is generally achieved using molecules such as surfactants, polymers, biomolecules, and polyaromatic compounds.¹⁰ The noncovalent interaction relies mainly on either hydrophobic^{5,11} or π - π interactions¹²⁻¹⁴ without any destruction of the π network integrity of the CNTs. Moreover, useful intrinsic properties such as optical, electrical, and mechanical properties are preserved and solubility is improved. However, the dynamic equilibrium nature of polymers on nanotube surfaces can be a hurdle for some applications, such as target-specific binding and drug delivery. Therefore, it is necessary to utilize the physicochemical properties of CNTs, such as PL and sidewalls of CNTs as a nano conduit, as the advanced strategies for biological applications.

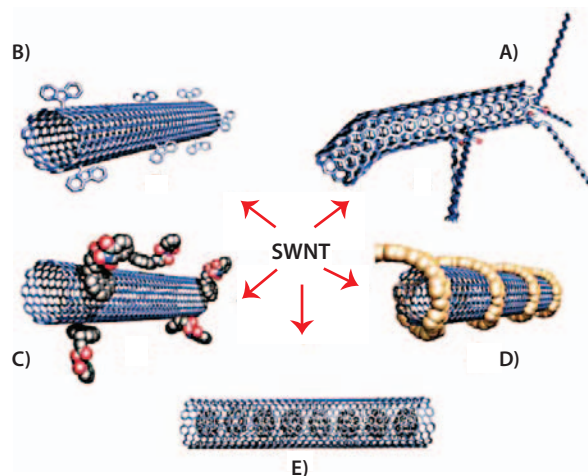


Figure 1. Functionalization strategies of SWNTs. Covalent functionalization using defect-group (A) and sidewall of SWNTs (B); noncovalent functionalization using noncovalent exohedral surfactants (C), noncovalent exohedral polymers (D), and endohedral C60 (E). Adapted from Reference 15.

Sorting Methods

The separation efficiency of CNTs based on the noncovalent approach strongly depends on the degree of bundling. Since a nanotube bundle contains a mixture of metallic and semiconducting tubes with various chiralities, it is important to first produce a high degree of chirality of individual CNTs; then improve the separation efficiency of CNTs afterward. Nanotube bundling can be monitored by absorbance and photoluminescence spectroscopies. Small bundling of nanotubes results in a red shift by up to tens of meV from the absorbance peak of nanotubes in the NIR region.¹⁶ The degree of bundling is also evaluated from the peak intensity of PL caused by the energy transfer found at the cross-point of two different CNTs, which is proportional to the bundling size of CNTs.¹⁷ The noncovalent separation methodologies are listed in Table 1.

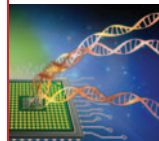


Table 1. Classifications, separation methodologies, and applications of SWNTs according to their type, chirality, handedness, diameter, and length.

Separation Degree	Type	Chirality	Handedness	Diameter	Length
Example					
Separation Methods	<ul style="list-style-type: none"> Electrophoresis Density gradient ultracentrifugation (DGU) Chromatography Selective solubilization Selective reaction 	<ul style="list-style-type: none"> DGU Chromatography Selective solubilization Selective reaction 	<ul style="list-style-type: none"> Electrophoresis DGU Chromatography Selective solubilization Selective reaction 	<ul style="list-style-type: none"> Electrophoresis DGU Chromatography Selective solubilization 	<ul style="list-style-type: none"> Electrophoresis DGU Chromatography Selective solubilization
Applications	<ul style="list-style-type: none"> Field effect transistors (FETs) Electronic devices Transparent electrode 	<ul style="list-style-type: none"> FETs Tuning PL for bio application 	<ul style="list-style-type: none"> Ballistic FETs 	<ul style="list-style-type: none"> Conductive film and thin film transistors (TFTs) CNT scanning tubes 	<ul style="list-style-type: none"> Conductive film and TFTs CNT scanning tubes

Examples of Sorting CNTs

Dielectrophoresis (DEP)

One of the initial efforts to sort CNTs by electronic type is the dielectrophoretic method.¹⁸ This process utilizes an alternating current (ac) DEP, where metallic nanotubes showing both a high dielectric constant and positive DEP are collected on the electrode for the high applied electric field, while semiconducting tubes having lower dielectric constant and negative DEP are left in the solvent. However, only small quantities of CNTs are collected by this method, and separation occurs solely by electronic type due to differences in polarizability in metallic and semiconducting CNTs.

DNA-based Ion Exchange Chromatography

This separation method is based on DNA-wrapped SWNTs, showing different electrostatic interactions with an ion exchange (IEX) column. A stable barrel is formed around the nanotubes with 2D H-bonding with single-stranded DNA (ssDNA) wrapped helically around individual CNTs (Figure 2A), exposing the deoxyribose phosphate. The selection of nanotubes is believed to originate from the electrostatic and electrodynamic interactions between the DNA barrel-nanotubes and the ion exchange resin.²³ Pure chiral nanotubes were separated by this method for the first time.⁴² A recent experiment showed the improved structural motive of ssDNA allows for separation of 12 different chiral CNTs with 60-90% purity (Figure 2B).²³ However, the estimated yield of chiral (*n, m*) tubes is very low; the majority of nanotubes are expected to be adsorbed onto the ion exchange column in a bundled state. A major drawback of SWNT separation by DNA-based ion exchange chromatography is the high cost of ssDNA used and expensive manufacturing process (i.e., high cost of the IEX column and its unavoidable replacement caused by clogging).

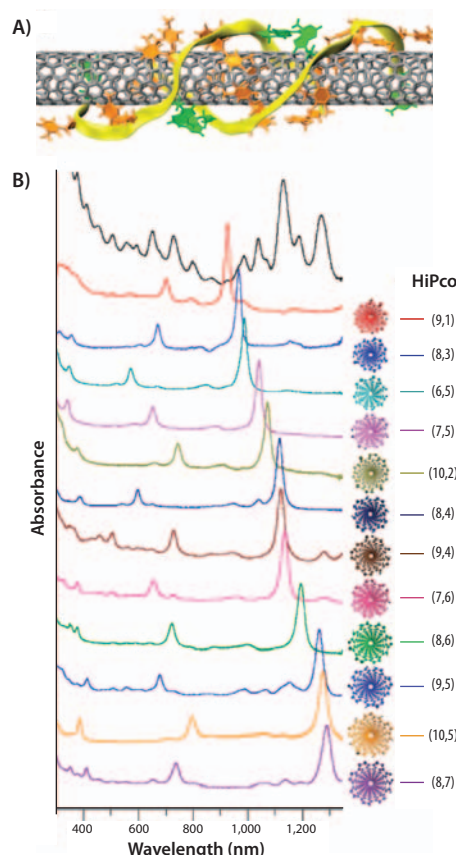


Figure 2. Separation of SWNTs using single-stranded DNA ribbons. **A)** Anti-parallel DNA (i.e., ATTTATTTATTT) strands wrap around (8,4) SWNT held by hydrogen bonding between DNA strands and π interaction between DNA and SWNTs. **B)** UV-Vis-NIR absorption spectra of 12 purified SWNTs with different chiralities separated by ion exchange column chromatography. Sorting of each SWNT can be enhanced by using different DNA sequences. Adapted from Reference 23.

Density Gradient Ultracentrifugation (DGU)

DGU separates nanotubes by the density difference of (n, m) CNTs in gradient medium using ultracentrifugation. CNTs dispersed in sodium cholate (or bile salt) exhibit different sediment coefficients according to their diameter, length, type (or metallicity), bundling, and even handedness.^{19,22,43} This method shows a variety of separation capabilities (Table 1). An example is illustrated in Figure 3, where color bands representing layer separation originate from the absorption of chiral CNTs. Iodixanol (Sigma Product No. D1556), an improved density gradient medium for DGU, allows adjustment of density from 1.32 (60%) to 1.00 g/cm³ (0%), which covers the range of densities from the bundled (1.2–1.3 g/cm³) to individualized (1.0 g/cm³) nanotubes from the dispersed samples. Introduction of a cosurfactant such as sodium dodecyl sulfate (SDS) enhances the selectivity of specific chirality.¹⁹ For example, ten pure nanotubes with purity from 34 to 88% have been separated by DGU with a cosurfactant.²² It is noteworthy that nanotubes with smaller diameters exhibit a lower density. Nanolntegris produces SWNTs with specific chirality via the DGU method, which are available through Aldrich Materials Science (Aldrich Product Nos. 750522 and 750530).

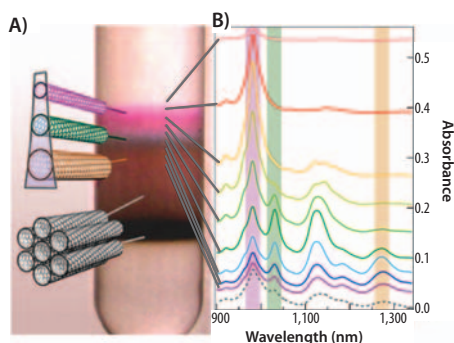


Figure 3. Sorting of SWNTs via density gradient ultracentrifugation (DGU). **A)** Upon ultracentrifugation (e.g., 200,000 *g*) using a swing bucket rotor, carbon nanotubes are sorted by their buoyancy (i.e., the highest buoyancy was exhibited from small diameter tubes) and are placed at their isopycnic point in the gradient gel. **B)** The corresponding NIR spectra of layered SWNTs after separation via DGU. Adapted from Reference 19.

Multi-column Gel Chromatography (MUGEC)

In MUGEC, several columns are connected vertically in series to obtain large-scale chirality separation. The selective adsorption of SWNTs dispersed in SDS on an allyl dextran-based gel column (Sephacryl® S-200HR, Sigma Product No. S200HR) allows for metallic vs. semiconducting separation and chirality-based separation of SWNTs. For thermodynamic reasons,⁴⁴ metallic tubes exhibit more stability toward the gel medium and are eluted first, while semiconducting tubes are preferentially adsorbed onto the gel medium (Figure 4A). This sorting method is also highly dependent on diameter and chirality similar to DGU. The separation order of multi-column gel chromatography shows the nanotubes with small diameter were adsorbed first on the gel, indicating a high affinity to the dextran medium. Figure 4B illustrates the separation of 13 types of nanotubes by purity.²⁴ This method is expected to provide relatively affordable chirality-pure nanotubes if a high-throughput separation is provided.

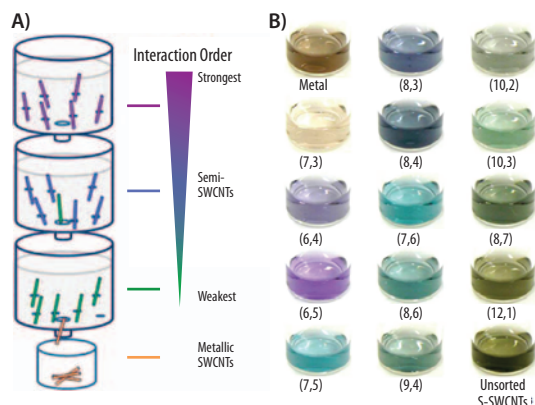


Figure 4. Chirality separation of SWNTs using allyl-dextran-based multi-column chromatography. **A)** Using SDS as a single surfactant, the dispersed SWNTs were adsorbed on column medium and, upon saturation, the single-chirality tubes are enriched according to its binding affinity toward the column. **B)** Bulk separation of iterative column chromatography to produce single chirality enriched SWNTs, showing their distinct colors according to their chirality. Adapted from Reference 24.

Flavin Mononucleotide (FMN)-based Titration

This method is comprised of the supramolecular helical wrapping of FMN onto a carbon nanotube surface (Figures 5A through 5C). This biomolecule exhibits distinct binding affinity or equilibrium constant toward cosurfactant titration, enabling (8,6) nanotube separation up to 85% purity (Figure 5D).²⁵ In addition, the optically active *d*-ribyl phosphate group of FMN provides a chiral sheath for the equally chiral nanotubes, resulting in nanotube separation with enantioselective handedness (Figure 5E).²⁶ Using the determined binding energy of FMN wrapping toward cosurfactant such as sodium dodecyl benzene sulfate (SDBS) on CNTs, this separation methodology might provide an affordable scale-up platform for selective CNTs.

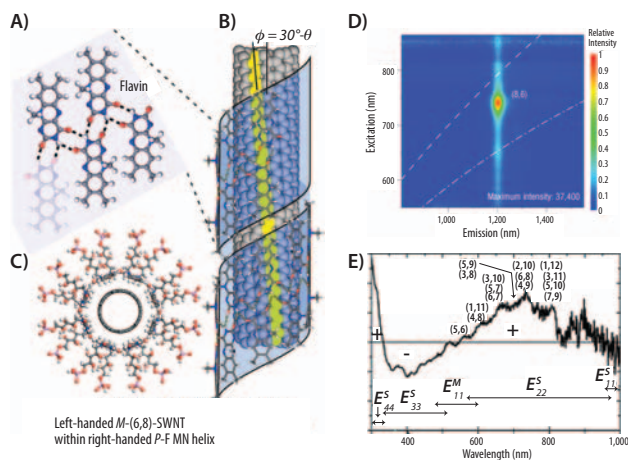
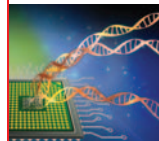


Figure 5. Flavin mononucleotide (FMN) self-organizes around SWNT through helical wrapping. **A)** 2D FMN sheet structure on the SWNT sidewall. One FMN forms quadruple hydrogen bonds with two facing FMNs. **B)** FMN possessing chiral *d*-ribyl phosphate group prefers left-handed SWNT within its own right-handed helical pattern. **C)** The phosphate side groups of FMNs impart SWNT dispersion by anionic repulsion. **D)** Photoluminescence mapping of separated (8,6) SWNT using dual-surfactant titration strategies. **E)** Circular dichroism spectrum of handedness of enantioselectively-separated SWNT using a dispersion of SWNT and FMN in aqueous solvents. Adapted from References 25,26.



Bio-application of Separated Carbon Nanotubes

CNTs have been used as novel biosensing platforms and nanoprobe for various biological targets. Many efforts employ CNTs as tools for cancer therapy. Clearly, surface chemistry, size, and degree of aggregation play critical roles in regulating CNTs' interaction with cells. Therefore, CNT separation techniques can provide valuable tools for tailored imaging and cancer therapeutics.

However, toxicity has been one of the major concerns for CNTs' use in biomedical applications. An *in vivo* study showed that CNTs functionalized with a polymer/surfactant seem to be safe even when orally fed to mice at a high dose (up to 1,000 mg/kg body weight).⁴⁵ It was reported that intratracheal administration of ground, unfunctionalized CNTs aggregate in the lungs and led to pulmonary toxicity and inflammation.⁴⁶ However, the aggregation effect (acute toxicity) was not observed for fluorescent individual SWNTs.⁴⁷

Bioimaging Utilizing CNTs

Bioimaging capability of CNTs relies on their fluorescence. Fluorescence is one of the relaxation pathways of photo-excited molecules, which can be relaxed via either radiative (fluorescent) or nonradiative channels. The radiative, fluorescence quantum yield of carbon nanotube ranges from 0.1% to 20%, depending on the kind of surfactants and media.^{5,48} Since most surfactants are not biologically compatible, it is necessary to use a biologically compatible lipid such as a phospholipid-polyethylene glycol⁴⁹ to attain the minimal dose of carbon nanotube.

Once nanotube-related biocompatibility and bundling issues are resolved, the separated CNTs require an adequate fluorescence range due to the strong absorption and scattering of human skin in the visible light region. It is desirable to utilize the near IR ranges (NIR I: 750-900 nm and NIR II: 1.0-1.4 μm),³⁸ where absorption coefficients of human dermis and subdermis are approximately 0.02 and 0.1 per mm, respectively.⁵⁰ It is known that near armchair nanotubes with smaller diameters have stronger photoluminescence.⁵¹ Recently, the Dai group demonstrated that chirality-enriched nanotubes (e.g., (12,1), and (11,3) tubes, **Figure 6A**) obtained via gel filtration method can be used for fluorescence in the NIR region. The separated nanotubes, whose excitation and emission are around 800 and 1,200 nm, respectively, not only enhances its fluorescence by 5-fold, but also provides a close match with an exciting NIR I laser line at 808 nm. Much brighter nanotubes significantly lower the dose of nanotube required, 0.16 mg/kg compared to a previous study using 1.0 mg/kg.³⁸ **Figure 6B** shows the NIR image of a mouse after injection of chirality-enriched CNTs and comparison with organs identified with principal component analysis (PCA) (**Figure 6C**).

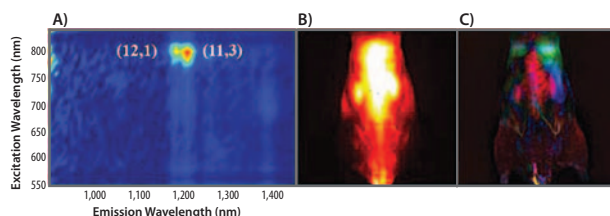


Figure 6. Real-time *in vivo* video imaging of whole mouse using chirality-enriched semiconducting SWNTs. **A)** PLE maps of chirality-sorted (12,1) and (11,3) SWNTs. **B)** *In vivo* whole mouse body imaging of NIR-II after injection of chirality-enriched SWNTs. **C)** Principal component analysis (PCA) image in which lungs, kidneys, and liver are color coded in green, pink, and blue, respectively. Adapted from Reference 39.

CNT-based Targeted Drug Delivery and Cancer Therapy

Covalently functionalized CNTs have been mainly used for *in vitro* targeted delivery vehicles for drugs, plasmid DNA, or small interfering RNA (siRNA) into cells by endocytosis. Covalent functionalization strategies for gene delivery utilize a primarily amine functionality of CNTs to stabilize anionic moieties of DNA. **Figure 7** illustrates various approaches for CNT-based drug delivery and cancer therapy. Primary functionalization approaches targeting the interaction with biological entities are: 1) for the functionalization of antibodies, peptides, and small interfering RNA (siRNA); and 2) CNTs designed as a vehicle for molecular (or drug) delivery. The former can be utilized to deliver target ligands, chemotherapy drugs, and biomolecules via facile covalent chemistry on the surfactant. The latter utilizes either cleavable covalent chemistry onto CNTs or noncovalent interactions, such as van der Waals interactions, between CNTs and the drug. A clear departure from these approaches was obtained utilizing functionalization of hydrophobic sidewalls of carbon nanotubes. As shown in **Figure 7**, an aromatic drug such as doxorubicin interacts with CNT sidewalls via π - π stacking. Sidewall functionalized CNTs can hold up to 4 grams of drug per 1 gram of nanotubes, owing to CNTs' large surface area. Interestingly, under an acidic pH environment, this drug favors the release of doxorubicin from the nanotube surface, which is suitable for treatment of tumor environment with local acidic environments.

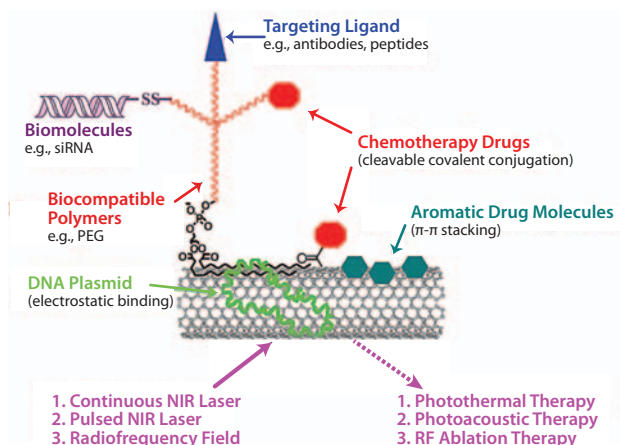
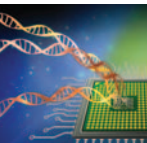


Figure 7. Schematic strategies of SWNTs-based drug-delivery and cancer therapy. Adapted from Reference 52.

In addition, CNTs can be used directly for the cancer therapy. Since photoexcited nanotubes relax by releasing thermal energy, this phenomenon can be utilized as photothermal therapy. If a short-pulsed laser is used, CNTs can act as nanobombs, when the incident power is beyond thermal conduction capability of nanotube, which is referred to photoacoustic therapy.⁵³ Another strategy is to generate heat from CNTs using a radio frequency (RF) field. Since near 13.6 MHz RF field has excellent tissue penetration ability,⁵⁴ this method can overcome the problems encountered by photothermal and photoacoustic therapies of CNTs.



Conclusion

Recent advances in sorting CNTs allow us to access chirality-pure carbon nanotubes with high purities. The separated CNTs, with their fine-tuned physical properties, can then be used in valuable, high-technology bioapplications. Although few examples of such applications are currently in use, appropriate carbon nanotubes with defined structure, electronic type, chirality, length, handedness, etc. show promising results for bioimaging, drug delivery, and other bio-related applications. Once the potential long-term toxicity of nanotubes is better understood, through a combination of photoluminescence, photothermal, and photoacoustic capabilities, CNTs will find extensive utility as tools for biomedical applications such as bioimaging, drug/gene delivery, and cancer therapy.

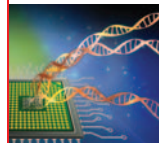
References

- Iijima, S. *Nature* **1991**, *354*, 56.
- Baughman, R. H.; Zakhidov, A. A.; de Heer, W. A. *Science* **2002**, *297*, 787.
- Kim, S. N.; Rusling, J. F.; Papadimitrakopoulos, F. *Advanced materials* **2007**, *19*, 3214.
- Saito, R.; Dresselhaus, G.; Dresselhaus, M. S. *Phys. Rev. B* **2000**, *61*, 2981.
- O'Connell, M. J.; Bachilo, S. M.; Huffman, C. B.; Moore, V. C.; Strano, M. S.; Haroz, E. H.; Rialon, K. L.; Boul, P. J.; Noon, W. H.; Kittrell, C.; Ma, J.; Hauge, R. H.; Weisman, R. B.; Smalley, R. E. *Science* **2002**, *297*, 593.
- Bachilo, S. M.; Balzano, L.; Herrera, J. E.; Pompeo, F.; Resasco, D. E.; Weisman, R. B. *J. Am. Chem. Soc.* **2003**, *125*, 11186.
- Bahr, J. L.; Tour, J. M. *J. Mater. Chem.* **2002**, *12*, 1952.
- Banerjee, S.; Hemraj-Benny, T.; Wong, S. S. *Adv. Mater.* **2005**, *17*, 17.
- Tasis, D.; Tagmatarchis, N.; Bianco, A.; Prato, M. *Chem. Rev.* **2006**, *106*, 1105.
- Gooding, J. J. *Electrochim. Acta* **2005**, *50*, 3049.
- Weisman, R. B.; Bachilo, S. M. *Nano Lett.* **2003**, *3*, 1235.
- Chen, R. J.; Zhang, Y.; Wang, D.; Dai, H. *J. Am. Chem. Soc.* **2001**, *123*, 3838.
- Nish, A.; Hwang, J.-Y.; Doig, J.; Nicholas, R. J. *Nat. Nanotechnol.* **2007**, *2*, 640.
- Peng, X.; Komatsu, N.; Bhattacharya, S.; Shimawaki, T.; Aonuma, S.; Kimura, T.; Osuka, A. *Nat. Nanotechnol.* **2007**, *2*, 361.
- Hirsch, A. *Angew. Chem. Int. Edit.* **2002**, *41*, 1853.
- Crochet, J.; Clemens, M.; Hertel, T. *J. Am. Chem. Soc.* **2007**, *129*, 8058.
- Tan, P. H.; Rozhin, A. G.; Hasan, T.; Hu, P.; Scardaci, V.; Milne, W. I.; Ferrari, A. C. *Phys. Rev. Lett.* **2007**, *99*, 137402.
- Krupke, R.; Hennrich, F.; von Lohneysen, H.; Kappes, M. M. *Science* **2003**, *301*, 344.
- Arnold, M. S.; Green, A. A.; Hulvat, J. F.; Stupp, S. I.; Hersam, M. C. *Nat. Nanotechnol.* **2006**, *1*, 60.
- Zheng, M.; Jagota, A.; Semke, E. D.; Diner, B. A.; McLean, R. S.; Lustig, S. R.; Richardson, R. E.; Tassi, N. G. *Nat. Mater.* **2003**, *2*, 338.
- Zheng, M.; Jagota, A.; Strano, M. S.; Santos, A. P.; Barone, P.; Chou, S. G.; Diner, B. A.; Dresselhaus, M. S.; Mclean, R. S.; Onoa, G. B.; Samsonidze, G. G.; Semke, E. D.; Usrey, M.; Walls, D. J. *Science* **2003**, *302*, 1545.
- Ghosh, S.; Bachilo, S. M.; Weisman, R. B. *Nat. Nanotechnol.* **2010**, *5*, 443.
- Tu, X.; Manohar, S.; Jagota, A.; Zheng, M. *Nature* **2009**, *460*, 250.
- Liu, H.; Nishide, D.; Tanaka, T.; Kataura, H. *Nat. Comm.* **2011**, *2*, 309.
- Ju, S.-Y.; Doll, J.; Sharma, I.; Papadimitrakopoulos, F. *Nat. Nanotechnol.* **2008**, *3*, 356.
- Ju, S.-Y.; Abanulo, D. C.; Badalucco, C. A.; Gascon, J. A.; Papadimitrakopoulos, F. *J. Am. Chem. Soc.* **2012**, *134*, 13196.
- Heller, D. A.; Mayrhofer, R. M.; Baik, S.; Grinkova, Y. V.; Usrey, M. L.; Strano, M. S. *J. Am. Chem. Soc.* **2004**, *126*, 14567.
- Moshhammer, K.; Hennrich, F.; Kappes, M. *Nano Res.* **2009**, *2*, 599.
- Marquis, R.; Greco, C.; Sadokierska, I.; Lebedkin, S.; Kappes, M. M.; Michel, T.; Alvarez, L.; Sauvajol, J.-L.; Meunier, S. p.; Mioskowski, C. *Nano Lett.* **2008**, *8*, 1830.
- Doorn, S. K.; Fields, R. E.; Hu, H.; Hamon, M. A.; Haddon, R. C.; Selegue, J. P.; Majidi, V. J. *Am. Chem. Soc.* **2002**, *124*, 3169.
- Fagan, J. A.; Becker, M. L.; Chun, J.; Hobbie, E. K. *Adv. Mater.* **2008**, *20*, 1609.
- Sun, X.; Zanic, S.; Darancioglu, D.; Welsher, K.; Lu, Y.; Li, X.; Dai, H. *J. Am. Chem. Soc.* **2008**, *130*, 6551.
- Li, H.; Zhou, B.; Lin, Y.; Gu, L.; Wang, W.; Fernando, K. A. S.; Kumar, S.; Allard, L. F.; Sun, Y.-P. *J. Am. Chem. Soc.* **2004**, *126*, 1014.
- Tans, S. J.; Verschueren, A. R. M.; Dekker, C. *Nature* **1998**, *393*, 49.
- Zhou, C.; Kong, J.; Yenilmez, E.; Dai, H. *Science* **2000**, *290*, 1552.
- Wu, Z.; Chen, Z.; Du, X.; Logan, J. M.; Sippel, J.; Nikolou, M.; Kamaras, K.; Reynolds, J. R.; Tanner, D. B.; Hebard, A. F.; Rinzler, A. G. *Science* **2004**, *305*, 1273.
- Zhang, L.; Tu, X.; Welsher, K.; Wang, X.; Zheng, M.; Dai, H. *J. Am. Chem. Soc.* **2009**, *131*, 2454.
- Welsher, K.; Sherlock, S. P.; Dai, H. *Proc. Natl. Acad. Sci.* **2011**, *108*, 8943.
- Diao, S.; Hong, G.; Robinson, J. T.; Jiao, L.; Antaris, A. L.; Wu, J. Z.; Choi, C. L.; Dai, H. *J. Am. Chem. Soc.* **2012**, *134*, 16971.
- Javey, A.; Guo, J.; Wang, Q.; Lundstrom, M.; Dai, H. *Nature* **2003**, *424*, 654.
- Asada, Y.; Miyata, Y.; Shiozawa, K.; Ohno, Y.; Kitauro, R.; Mizutani, T.; Shinohara, H. *J. Phys. Chem. C* **2010**, *115*, 270.
- Zheng, M.; Semke, E. D. *J. Am. Chem. Soc.* **2007**, *129*, 6084.
- Fagan, J. A.; Becker, M. L.; Chun, J.; Nie, P.; Bauer, B. J.; Simpson, J. R.; Hight-Walker, A.; Hobbie, E. K. *Langmuir: the ACS journal of surfaces and colloids* **2008**, *24*, 13880.
- Hirano, A.; Tanaka, T.; Kataura, H. *ACS nano* **2012**.
- Kolosnjaj-Tabi, J.; Hartman, K. B.; Boudjemaa, S.; Ananta, J. S.; Morgant, G.; Szwarc, H.; Wilson, L. J.; Moussa, F. *ACS nano* **2010**, *4*, 1481.
- Muller, J.; Huaux, F.; Moreau, N.; Misson, P.; Heilier, J. F.; Delos, M.; Arras, M.; Fonseca, A.; Nagy, J. B.; Lison, D. *Toxicol. Appl. Pharmacol.* **2005**, *207*, 221.
- Mutlu, G. M.; Budinger, G. R. S.; Green, A. A.; Ulrich, D.; Soberanes, S.; Chiarella, S. E.; Alheid, G. F.; McCrimmon, D. R.; Szeifler, I.; Hersam, M. C. *Nano Lett.* **2010**, *10*, 1664.
- Ju, S.-Y.; Kopcha, W. P.; Papadimitrakopoulos, F. *Science* **2009**, *323*, 1319.
- Welsher, K.; Liu, Z.; Sherlock, S. P.; Robinson, J. T.; Chen, Z.; Darancioglu, D.; Dai, H. *Nat Nano* **2009**, *4*, 773.
- Simpson, C. R.; Kohl, M.; Essenpreis, M.; Cope, M. *Phys. Med. Biol.* **1998**, *43*, 2465.
- Oyama, Y.; Saito, R.; Sato, K.; Jiang, J.; Samsonidze, G. G.; Gruneis, A.; Miyauchi, Y.; Maruyama, S.; Jorio, A.; Dresselhaus, G.; Dresselhaus, M. S. *Carbon* **2006**, *44*, 873.
- Liu, Z.; Robinson, J. T.; M. S.; Tabakman; Yang, K.; Dai, H. *Mater. Today* **2011**, *14*, 316.
- Kang, B.; Yu, D. C.; Dai, Y. D.; Chang, S. Q.; Chen, D.; Ding, Y. T. *Small* **2009**, *5*, 1292.
- Gannon, C. J.; Cherukuri, P.; Jakobson, B. I.; Cognet, L.; Kanzius, J. S.; Kittrell, C.; Weisman, R. B.; Pasquali, M.; Schmidt, H. K.; Smalley, R. E.; Curley, S. A. *Cancer* **2007**, *110*, 2654.

Single-walled Carbon Nanotubes (SWNT)

For a complete list of available materials, visit aldrich.com/swnt.

Purity	Dimensions	Production Method	Prod. No.
>95% (carbon as SWNT)	diameter 0.6 - 1.1 nm	CoMoCAT® Catalytic Chemical Vapor Deposition (CVD) method	775533-250MG 775533-1G
≥93% (carbon as SWNT), (6,5) chirality	diameter 0.7 - 0.9 nm (by fluorescence)	CoMoCAT® Catalytic Chemical Vapor Deposition (CVD) Method	773735-250MG 773735-1G
≥77% (carbon as SWNT), (7,6) chirality	diameter 0.7 - 1.1 nm, L 300-2300 nm (mode: 800nm; AFM)	CoMoCAT® Catalytic Chemical Vapor Deposition (CVD) Method	704121-250MG 704121-1G
≥77% (carbon as SWNT), (6,5) chirality	diameter 0.7 - 0.9 nm (by fluorescence), L ≥700 nm	CoMoCAT® Catalytic Chemical Vapor Deposition (CVD) Method	704148-250MG 704148-1G
≥77% (carbon as SWNT)	diameter 0.7 - 1.4 nm	CoMoCAT® Catalytic Chemical Vapor Deposition (CVD) Method	724777-250MG 724777-1G
≥70% (carbon as SWNT)	diameter 0.7 - 1.3 nm, L 450-2300 nm (mode: 800nm; AFM)	CoMoCAT® Catalytic Chemical Vapor Deposition (CVD) Method	704113-250MG 704113-1G
>70% TGA	average diameter 2 nm, × L × 3 (TEM)	Catalytic Carbon Vapor Deposition (CCVD) Method	755710-250MG 755710-1G
30% (Metallic) 70% (Semiconducting)	diameter 1.2 - 1.7 nm, L 0.3-5 μm	Electric Arc Discharge Method	750492-100MG
30% (Metallic) 70% (Semiconducting)	diameter 1.2 - 1.7 nm, L 0.3-5 μm	Electric Arc Discharge Method	750514-25MG
2% (Metallic) 98% (Semiconducting)	diameter 1.2 - 1.7 nm, L 0.3-5 μm	Electric Arc Discharge Method	750522-1MG
2% (Semiconducting) 98% (Metallic)	diameter 1.2 - 1.7 nm, L 0.3-5 μm	Electric Arc Discharge Method	750530-1MG
40-60 wt. % carbon basis	D × L 2-10 nm × 1-5 μm (bundle dimensions) 1.3-1.5 nm (individual SWNT diameter)	Electric Arc Discharge Method	698695-1G 698695-5G



Double-walled Carbon Nanotubes (DWNT)

For a complete list of available materials, visit aldrich.com/dwnt.

Purity	Dimensions	Production Method	Prod. No.
Metal Oxide \leq 10% TGA	avg. diam. \times L 3.5 nm \times $>$ 3 μ m (TEM)	Catalytic Carbon Vapor Deposition (CCVD) Method	755141-1G
Metal Oxide $<$ 10% TGA	avg. diam. \times L 3.5 nm \times 1-10 μ m (TEM)	Catalytic Carbon Vapor Deposition (CCVD) Method	755168-1G
50-80% carbon basis	O.D. \times I.D. \times L 5 nm \times 1.3-2.0 nm \times 50 μ m	Chemical Vapor Deposition (CVD) Method	637351-200MG 637351-1G

Multi-walled Carbon Nanotubes (MWNT)

For a complete list of available materials, visit aldrich.com/mwnt.

Purity	Description	Production Method	Prod. No.
\geq 98% carbon basis	O.D. \times I.D. \times L 10 nm \pm 1 nm \times 4.5 nm \pm 0.5 nm \times 3-6 μ m (TEM)	CoMoCAT [®] Catalytic Chemical Vapor Deposition (CVD) Method	773840-25G 773840-100G
$>$ 95% (carbon)	O.D. \times L 6-9 nm \times 5 μ m diam. 6.6 nm (median) diam. 5.5 nm (mode)	CoMoCAT [®] Catalytic Chemical Vapor Deposition (CVD) Method	724769-25G 724769-100G
Metal Oxide $<$ 5% TGA	avg. diam. \times L 9.5 nm \times $<$ 1 μ m (TEM), thin and short	Catalytic Carbon Vapor Deposition (CCVD) Method	755117-1G
Metal Oxide $<$ 5% TGA	avg. diam. \times L 9.5 nm \times 1.5 μ m (TEM), thin	Catalytic Carbon Vapor Deposition (CCVD) Method	755133-5G
$>$ 98% carbon basis	O.D. \times L 6-13 nm \times 2.5-20 μ m 10 μ m (average length, TEM) 12 nm (average diameter, HRTEM)	Chemical Vapor Deposition (CVD) Method	698849-1G
$>$ 90% carbon basis	D \times L 110-170 nm \times 5-9 μ m	Chemical Vapor Deposition (CVD) Method	659258-2G 659258-10G
20-30% MWCNT basis	O.D. \times L 7-12 nm \times 0.5-10 μ m, powdered cylinder cores	Electric Arc Discharge Method	406074-500MG 406074-1G 406074-5G
$>$ 7.5% MWCNT basis	O.D. \times L 7-15 nm \times 0.5-10 μ m, as-produced cathode deposit	Electric Arc Discharge Method	412988-100MG 412988-2G 412988-10G
$>$ 95 atom % carbon basis (x-ray)	diam. \times L 100-150 nm \times 30 μ m (SEM), vertically aligned on silicon wafer substrate	Plasma-Enhanced Chemical Vapor Deposition (PECVD) Method	687804-1EA
$>$ 99.9% carbon basis	diam. \times L 100 nm \pm 10% \times 30 μ m \pm 10%, vertically aligned on copper wafer substrate	Plasma-Enhanced Chemical Vapor Deposition (PECVD) Method	687812-1EA

Functionalized Nanotubes

For a complete list of available materials, visit aldrich.com/cnt.

Name	Structure	Purity	Dimensions	Production Method	Prod. No.
Carbon nanotube, single-walled, carboxylic acid functionalized		$>$ 90% carbon basis	D \times L 4-5 nm \times 0.5-1.5 μ m (bundle dimensions)	Electric Arc Discharge Method	652490-250MG 652490-1G
Carbon nanotube, multi-walled, carboxylic acid functionalized		$>$ 80% carbon basis	avg. diam. \times L 9.5 nm \times 1.5 μ m	Catalytic Carbon Vapor Deposition (CCVD) Method	755125-1G
Carbon nanotube, single-walled, poly(ethylene glycol) functionalized		$>$ 80% carbon basis	D \times L 4-5 nm \times 0.5-0.6 μ m (bundle dimensions)	Electric Arc Discharge Method	652474-100MG
Carbon nanotube, single-walled, amide functionalized		$>$ 90% carbon basis	D \times L 4-6 nm \times 0.7-1.0 μ m (bundle dimensions)	Electric Arc Discharge Method	685380-100MG
Carbon nanotube, single-walled, octadecylamine functionalized		80-90% carbon basis	D \times L 2-10 nm \times 0.5-2 μ m (bundle dimensions)	Electric Arc Discharge Method	652482-100MG
Carbon nanotube, single-walled, polyaminobenzene sulfonic acid functionalized		75-85% carbon basis	D \times L 1.1 nm \times 0.5-1.0 μ m (bundle dimensions)	Electric Arc Discharge Method	639230-100MG

Polydiacetylene Nanotubes (PDNT)

The World's First Commercially Available Nanotubes Based on Lipid Diacetylene Materials

Properties

- Extremely uniform inner and outer diameter of nanotubes—highly pure
- Photo- and electro-conductive
- Thermo- and mechano-chromism

Potential Applications

- Biosensors for viruses, bacteria, and glucose
- Colorimetric pressure sensors
- Neuronal networks, enzyme carrier
- Nanoelectronics and Lab-on-a-chip
- Langmuir-Blodgett films
- MEMS, membrane filtration, and gas separation

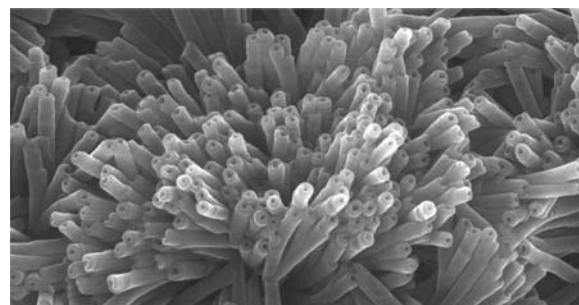
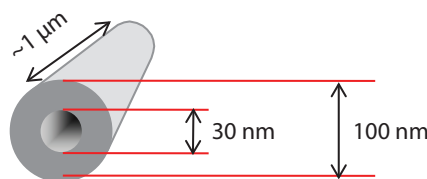


Figure 1. Uniform diameter

Aldrich Prod. No. 773492



Aldrich Prod. No. 773484

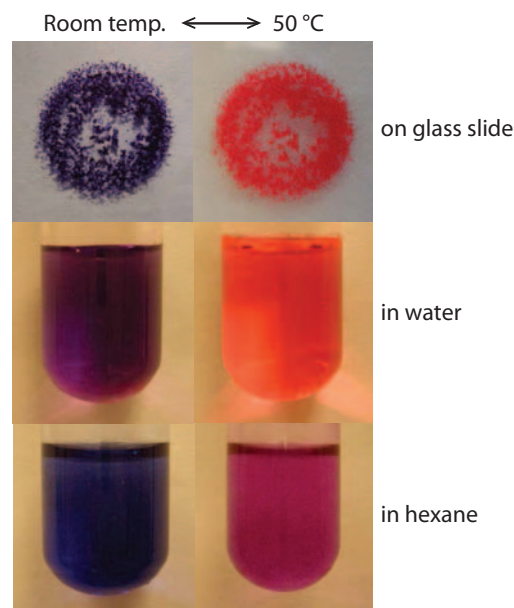
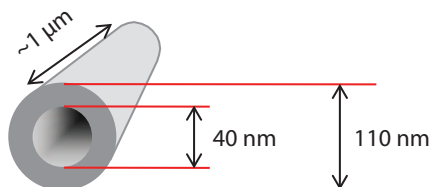


Figure 2. Unique chromism

To explore our nanotube materials, visit aldrich.com/cnt

Graphene in Biotechnology



Alba Centeno and Amaia Zurutuza Elorza*
Graphenea S.A.
Tolosa Hiribidea, 76, E-20018 Donostia - San Sebastian, Spain
*Email: a.zurutuza@graphenea.com

Graphene Technology

Graphene has emerged as the new wonder material. Being only one atom thick and composed of carbon atoms arranged in a hexagonal honeycomb lattice structure, the interest in this material has exploded exponentially since 2004 when it was first isolated and identified using a very simple method.¹

Graphene is the building block for carbon nanomaterials with different dimensionalities (Figure 1). For example, if graphene is wrapped up into a ball, a 0D fullerene is obtained; when rolled, a 1D nanotube; and if stacked, a 3D graphite is obtained.

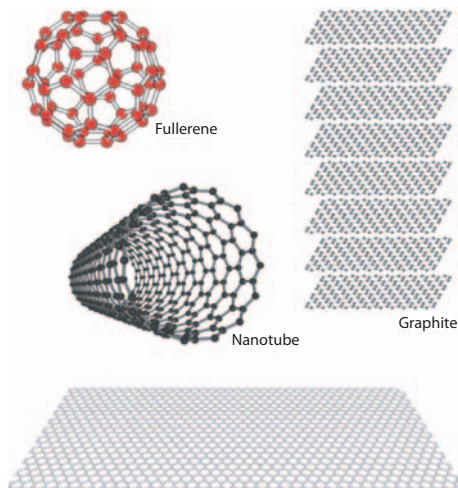


Figure 1. Graphene is the building block for other carbon materials.

The carbon atoms in graphene exhibit sp^2 hybridization and this hybridization together with the atomic thickness (0.345 nm), give this unique material extraordinary properties, such as: extremely high electron and hole mobility values ($>10^5 \text{ cm}^2\text{V}^{-1}\text{s}^{-1}$) even at room temperature;² very high thermal conductivity ($>4,000 \text{ Wm}^{-1}\text{K}^{-1}$) at room temperature;³ 2.3% of light absorbance over a wide range of the visible spectrum;⁴ mechanical strength 300 times higher than steel with a Young's modulus of 1 TPa (when compared to steel with the same thickness);⁵ and an impermeability to gases, including helium.⁶ It is expected graphene will find application in many different fields such as electronics, optoelectronics, energy (solar, batteries, supercapacitors), touch screen and display technology, lighting, and composites.

Moreover, graphene and its derivatives have a great potential for biomedical applications since their properties (such as high surface area, tailor-made functionality, and a large sp^2 hybridization surface) provide excellent biocompatibility, physiological solubility, stability, and capability of loading or conjugating different types of compounds. Table 1 summarizes the advantages of graphene and suitable forms in

biotechnology applications. It is important to note graphene can be synthesized in two different forms: 1) film via chemical vapor deposition (CVD); and 2) powder via chemical exfoliation: graphene oxide (GO) and reduced graphene oxide (rGO). Depending on the form, the properties of the graphene will vary.

Graphene in Biomedical Applications

Molecules, biomolecules, quantum dots, polymers, and even nanoparticles could be loaded/conjugated onto graphene-based carriers (Figure 2). The loading could be achieved via covalent bonding or non-covalent interactions; e.g., hydrogen bonding, hydrophobic, π - π stacking, and electrostatic interactions.

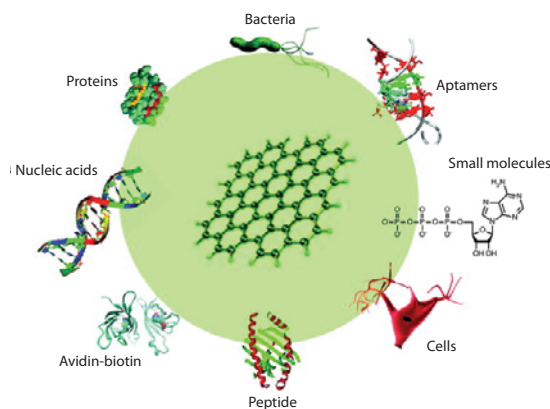


Figure 2. Biofunctionalization of graphene and its derivatives.⁷ Reprinted with permission from Elsevier.

Graphene Oxide in Drug and Gene Delivery

Graphene and its derivatives are the latest materials to be designed for drug and gene delivery applications, including targeted delivery. The ability to load both water-soluble and insoluble active compounds, and attach different targeting moieties onto graphene oxide (GO) platelets could enable their use in targeted or non-targeted drug and gene delivery applications.

Functionalization of the GO platelets is extremely important to improve biocompatibility and solubility of graphene, and also to achieve successful targeted delivery and diverse therapeutic treatments. The most common strategy for the chemical modification of the GO platelets is covalent attachment of polymers. Many different polymeric moieties have been successfully grafted onto GO, including polyethylene glycol (PEG, Aldrich Product No. 81300), chitosan (Aldrich Product No. 448869) and polyethyleneimine (PEI, Aldrich Product No. 482595). In addition to polymers, biotargeting ligands, DNA, proteins, bacteria, cells, quantum dots, and nanoparticles have also been grafted onto graphene and its derivatives. Therefore, the structural features and ease of chemical modification make GO a very versatile platform for biomedical applications.

Since many pharmaceutically active compounds contain aromatic groups, they could be stabilized via π - π interactions with graphene. For example, doxorubicin (DOX), an anticancer drug, was loaded via π - π stacking onto PEGylated nano-GO (NNGO) (lateral dimensions $<10 \text{ nm}$) functionalized with an antibody for *in vitro* targeted drug delivery.⁸

In order to enhance anticancer efficiency and target tumor tissues and associated cells, a dual-targeting drug delivery system based on a multifunctionalized GO was developed.⁹ The GO was functionalized with folic acid (FA) molecules for molecular targeting and magnetic iron oxide (Fe_3O_4) nanoparticles (Aldrich Product No. 725331) for magnetic targeting. First, the (3-aminopropyl)triethoxysilane (APS) (Aldrich Product No. 741442) modified superparamagnetic GO- Fe_3O_4 nano-hybrids were prepared, followed by conjugation of FA onto the Fe_3O_4 nanoparticles via imide linkages between the amino groups of the APS and the carboxylic groups of the FA. In the final step, DOX was loaded onto these multifunctionalized carriers via π - π stacking, shown in Figure 3. Fluorescein isothiocyanate (FITC, Sigma Product No. F7250) was used for labeling. The results indicated the potential of these multifunctional GO-based carriers for the targeted delivery and controlled release of anticancer drugs. In addition, the DOX release could be controlled by pH conditions in the surrounding environment.

Alternatively, photothermal treatment could be combined with anti-cancer drugs to improve the therapeutic efficacy.¹⁰ Photothermal therapy with DOX-loaded PEGylated NGO was tested *in vivo* in a preclinical mouse model. The combination of photothermal therapy and chemotherapy significantly improved the efficacy of cancer treatment in comparison with either therapy alone. In a second *in vivo* study, the DOX was loaded onto GO-based carriers that included a molecular targeting moiety (FA-modified β -cyclodextrin).¹¹ In both studies, the functionalized GO drug delivery systems performed better than DOX alone *in vivo* due to better efficacy and reduced number of side effects, which in turn led to an improved mortality rate. In a recent study, a combination of magnetically targeted drug delivery, photothermal therapy, and magnetic resonance imaging (MRI) was investigated.¹²

One major challenge facing gene delivery is the development of a safe gene vector that protects DNA from degradation and enables cellular uptake of DNA with high efficiency. Recent studies have revealed PEI-modified GO not only significantly lowered the cytotoxicity of PEI, but also improved its transfection efficiency for efficient DNA delivery.^{13,14} Furthermore, in one of the studies, DNA could be delivered into the cell nucleus, as evidenced by intracellular tracking of the reporter gene.¹⁴

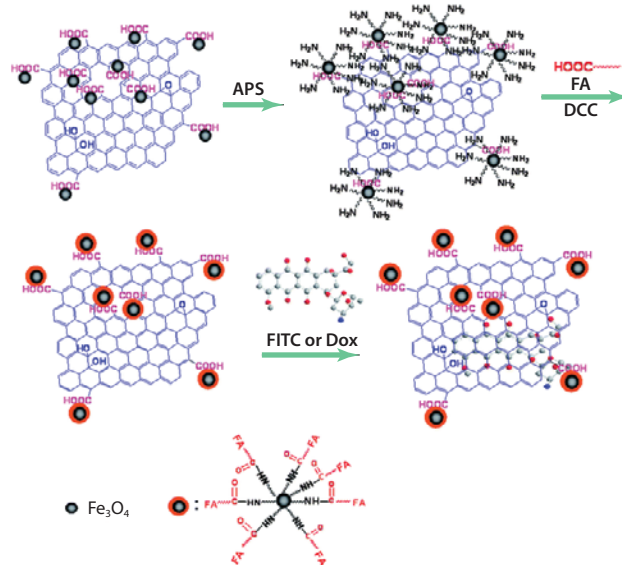


Figure 3. Multifunctional GO based carrier.⁹ Reproduced by permission of The Royal Society of Chemistry.

Table 1. Graphene in biotechnology applications

Application	Suitable Form	Advantages
Drug and gene delivery	GO & rGO platelets	<ul style="list-style-type: none"> Excellent biocompatibility, physiological solubility, and stability Capability of loading various molecules
Tissue engineering	Graphene films/GO & rGO platelets	<ul style="list-style-type: none"> Biocompatibility Elasticity and flexibility Adaptability Functionality
Molecular imaging	GO & rGO platelets	<ul style="list-style-type: none"> Excellent biocompatibility, physiological solubility, and low cytotoxicity Unique optical properties (NIR region, decreased interference from cells, organs, or tissues) Greater bio-detection and imaging efficiency
Electrochemical biosensors	Graphene films/rGO platelets	<ul style="list-style-type: none"> Low charge transfer resistance Fast electron transfer kinetics Low background noise High signal-to-noise ratio
Optical biosensors (Fluorescence resonance energy transfer, FRET)	GO platelets	<ul style="list-style-type: none"> Superior quenching efficiency, ability to quench electron donors Adsorption of ssDNA Low background noise High signal-to-noise ratio Protection from enzymatic cleavage Transportation capability in living cells & <i>in vivo</i> systems
Electrical biosensors (Field effect transistor, FET)	Graphene films	<ul style="list-style-type: none"> Low thermal and electrical noise Lower detection limit Capability to detect both positively & negatively charged species due to bipolar nature
Bioelectronics, implants	Graphene films	<ul style="list-style-type: none"> High electron mobility, biocompatibility, flexibility, adaptability
TEM supports	Graphene films	<ul style="list-style-type: none"> Atomic thickness, enhanced contrast, direct imaging of organic molecules Atomic level visualization of static and dynamic phenomena



Graphene Films, Graphene Oxide, and Reduced Graphene Oxide in Tissue Engineering

Tissue engineering relies on the design of biocompatible scaffolds with suitable physical, chemical, and mechanical properties. Graphene and its derivatives are of interest as scaffold materials due to their inherent elasticity, flexibility, high surface area, adaptability, and functionality. GO and rGO, in the form of thin films, were shown to be appropriate scaffolds for the growth of mammalian fibroblast cells since they display good biocompatibility as a surface coating material, without inducing notable detrimental effects while enhancing some cellular functions such as gene transfection and expression.¹⁵

Furthermore, growth and proliferation of human stem cells has been observed on various graphene-coated platforms.¹⁶ Single-layer graphene grown via CVD was transferred onto polydimethyl siloxane (PDMS) (Aldrich Product Nos. 761028 and 761036), polyethylene terephthalate (PET), glass, and silicon/silicon dioxide (Si/SiO₂) platforms. Graphene was found to be a very promising biocompatible scaffold, regardless of the underlying platform, that promoted the proliferation of human mesenchymal stem cells (hMSCs) and accelerated their specific differentiation into bone cells. Figure 4A depicts a CVD graphene film that has been transferred onto a Si/SiO₂ platform. Bone cell formation, indicated by specific immunostaining for osteocalcin (OCN), occurred only on the graphene film while no bone cells were formed on the Si/SiO₂ platform (Figure 4B). Alizarin red staining indicates the presence or absence of calcium deposits due to bone nodule formation and can be used for quantitative measurements. Quantification of results are shown in Figures 4C and 4D, where the extent of calcium deposition on the various scaffolds was compared. Calcium deposition was found to be greatest on graphene films, independent of the platform, and even in the absence of the growth factor BMP-2. In order to confirm these results, the effect to induce bone cell differentiation of graphene and BMP-2 were compared. In the absence of both graphene and BMP-2, no bone nodule formation was detected (Figure 4E) since negative alizarin red staining was obtained. With the addition of BMP-2, positive staining was observed (Figure 4G). Graphene-coated PET also showed positive staining, even in the absence of BMP-2 (Figure 4F). Positive staining was also obtained in the presence of both BMP-2 and graphene (Figure 4H). Remarkably, graphene accelerated cell differentiation, even in the absence of commonly used growth factors. Therefore, the incorporation of graphene films in implants or injured tissues would not affect the physiological conditions of the surrounding microenvironment.¹⁶

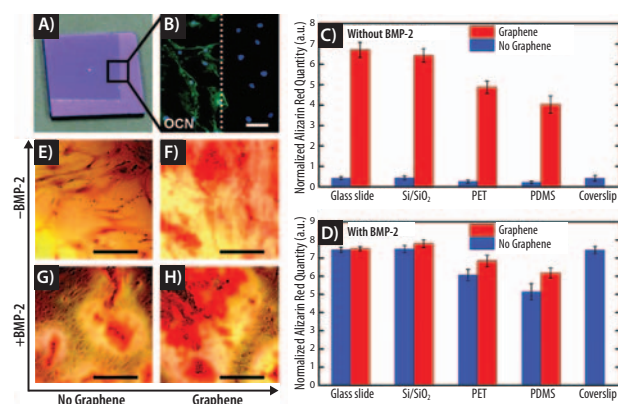


Figure 4. Graphene accelerates bone cell differentiation. **A)** Optical image of CVD graphene on Si/SiO₂, showing the graphene boundary. **B)** OCN marker indicates bone cell formation only on the graphene area. **C)** Cells grown in the absence of BMP-2. **D)** Cells grown in the presence of BMP-2. **E-H)** PET substrate stained with alizarin red reveal calcium deposits due to osteogenesis. **E)** PET without BMP-2 and without graphene. **F)** PET without BMP-2 and with graphene. **G)** PET with BMP-2 and without graphene. **H)** PET with both BMP-2 and graphene. Scale bars 100 μm. Reprinted with permission from reference 16. Copyright 2011 American Chemical Society.

Graphene films produced via CVD were found to enhance differentiation of human neural stem cells to neurons (hNSCs) rather than glia.¹⁷ The hNSCs adhered to graphene rather than glass and differentiated mainly into neural cells. These results open up many opportunities for graphene in neuroscience and other fields, including stem cell research and regenerative medicine.

In another study, GO and graphene films produced via CVD were tested in the proliferation and subsequent differentiation of stem cells (hMSCs) into specific tissues.¹⁸ Graphene films were found to proliferate and differentiate stem cells (hMSCs) into osteogenic tissue in the presence of osteogenic chemical inducers. GO enhanced adipogenic differentiation of the stem cells. It was found GO and graphene films were effective preconcentration scaffolds for accelerated stem cell growth and differentiation through molecular interactions.¹⁸

Graphene Oxide and Reduced Graphene Oxide in Molecular Imaging

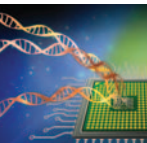
GO was used as a fluorescent marker for intracellular imaging studies via optical imaging. PEGylated nano-GO (NGO) was found to be photoluminescent in the visible and infrared regions.⁸ Intrinsic photoluminescence of GO enabled NIR imaging of lymphoma cells after molecular targeting of the PEGylated NGO. In other reports, fluorescein-functionalized PEGylated NGO and gelatin-grafted rGO labeled with rhodamine 6G (fluorescent dye, Aldrich Product No. 252433) were used for cellular imaging.^{19,20} In both cases, the PEG and gelatin linkers prevented GO and rGO from quenching the conjugated fluorescein and rhodamine, respectively.

rGO-based quantum dots were tested as intracellular fluorescent probes in human carcinoma cells (MG-63, HeLa, Sigma Product No. 86051601).²¹⁻²³ These materials were prepared either via a one-step solvothermal method starting from GO²¹ or rGO conjugated with quantum dots (QDs) using a bridge of bovine serum albumin (BSA, Sigma Product No. A7888),²² or PEG and FA as the molecular targeting moiety.²³ The nanocomposites combined the capability of cell tumor bioimaging and photothermal therapy, since they could absorb NIR irradiation, as demonstrated by *in vitro* and *in vivo* studies. The integration of these functionalities could open up excellent opportunities in cancer diagnosis, imaging, and treatment combined.

Even though most of the reported optical imaging studies were carried out *in vitro*, a few *in vivo* studies have been described. PEGylated NGO (lateral dimensions 10-50 nm) was conjugated with a NIR fluorescent dye for *in vivo* fluorescence imaging followed by photothermal therapy in mouse tumor models.²⁴ The results show highly efficient tumor passive targeting and relatively low retention in the reticuloendothelial system. No noticeable toxicity effects were detected in the mice. PEGylated NGO was found to have very good biocompatibility.

PEG and dextran-coated iron oxide-GO nanocomposites as T₂ contrast agents *in vivo* and *in vitro* MRI studies, respectively, were reported.^{12,25} The *in vivo* study showed PEG-coated iron oxide-GO nanoparticles accumulated in tumor and liver areas.¹² High uptake by the tumor was attributed to the enhanced permeability and retention effect of cancerous tumors. Compared to iron oxide nanoparticles alone, the nanocomposite materials exhibited enhanced cellular MRI imaging performance.²⁵

Positron emission tomography (PET) is a very sensitive imaging technique that requires small concentrations of isotopes. A radiolabeled antibody conjugated PEGylated NGO was investigated for *in vivo* targeting and PET imaging of tumor vasculature in a mouse model of breast cancer.²⁶ It was demonstrated functionalized NGO could be specifically directed to the tumor vasculature *in vivo* through targeting of endoglin (CD105, Sigma Product No. SRP6015), a vascular marker for tumor angiogenesis.



Graphene in Biosensors/Bioelectronics

Graphene Oxide and Reduced Graphene Oxide in Biosensors

Graphene's unique electrochemical properties include a wide electrochemical window, low-charge transfer resistance, well-defined redox peaks, and rapid electron transfer kinetics. As a result, graphene could be very suitable as an electrode material in electrochemical biosensors. Another important feature required in optical biosensors is its ability to be functionalized. As previously mentioned, graphene and especially GO are very versatile materials for further functionalization.

rGO-based electrodes have been the primary form of graphene reported in electrochemical biosensor studies since a certain conductivity is required to function as an electrode. Due to their high surface area, they have a high loading capacity leading to increased sensitivity. In addition, the role of graphene is to reduce the electron transfer distance between the active sites of the biomolecules and the electrode area. Therefore, a certain functionality could lead to more favorable interactions with the biomolecules. Electrochemical biosensors with rGO-based electrodes were reported to detect a variety of biomolecules ranging from DNA, glucose, ethanol, dopamine, ascorbic acid, uric acid, and acetaminophen (APAP).²⁷ They were able to detect all four DNA bases in both single-stranded DNA (ssDNA) and double-stranded DNA (dsDNA). It has been reported graphene-based glucose biosensors exhibit good sensitivity, selectivity, and reproducibility.^{28,29} In addition, cytochrome c, nicotinamide adenine dinucleotide (NADH, [Sigma Product No. N8535](#)), hemoglobin ([Sigma Product No. H7379](#)), horseradish peroxidase (HRP), and cholesterol biosensors have been developed using rGO-based electrodes.²⁸ To the best of our knowledge, CVD graphene films have not been reported in these types of biosensors; however, due to their superior electronic properties and atomic thickness it seems an obvious choice to be used as electrode material.

Among optical biosensors, fluorescence resonance energy transfer (FRET)-type biosensors have been widely reported using graphene and its derivatives. FRET involves the transfer of energy from a donor fluorophore to an acceptor fluorophore. Graphene and its derivatives provide certain benefits in this process, including a high signal-to-noise ratio due to a low background and protection from enzymatic cleavage. Graphene and GO have shown strong interactions with nucleic acids through π - π stacking. ssDNA can be adsorbed onto GO, while dsDNA cannot be stably adsorbed due to an efficient shielding of the nucleobases within the negatively charged dsDNA phosphate backbone. Typically, fluorescent molecules attached to ssDNA are conjugated onto GO for the fabrication of a FRET biosensor. Depending on the utilized probes (e.g., ssDNA, aptamer, and molecular beacon [MB]), different targets (e.g., cDNA, human thrombin, Ag^+ , bovine thrombin, surviving mRNA, and Au nanoparticle-labeled cDNA) can be detected.⁷ The incorporation of GO into an MB-based FRET biosensor increased the sensitivity and single-base mismatch selectivity for the target DNA.³⁰ By incorporating aptamers as probes, the targeting field of graphene-based FRET biosensors could be extended from DNA to ions (Ag^+), small molecules, and proteins (bovine thrombin, [Sigma Product No. T9549](#)).⁷

Graphene Films in Bioelectronics

Field effect transistor (FET)-based biosensors can offer higher sensitivity, with rapid response, nanoscale fabrication procedures and nanoscale device dimensions over other types of electrochemical sensors. FET-based biosensors have been fabricated mainly using graphene films synthesized via CVD and mechanically exfoliated graphene flakes, due to their superior electronic properties. Mechanically exfoliated graphene flakes were investigated in electrolyte-gated FETs for the detection of label-free BSA.³¹ A pH-dependent conductance was observed, indicating their potential use as pH sensors. A flexible glucose FET biosensor

fabricated using CVD graphene showed ambipolar transfer characteristics.³² In this work, the graphene film was deposited on flexible PET platforms and functionalized with glucose oxidase (GOD) to form a solution-gated FET biosensor (**Figure 5**). The graphene FET could be applied in portable, wearable and implantable glucose level monitoring applications.

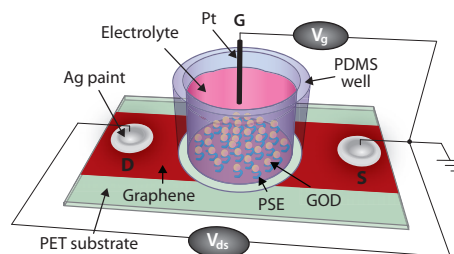


Figure 5. CVD graphene-based FET biosensor. Adapted from Reference 32.

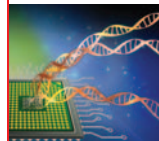
Furthermore, large area graphene grown by CVD was shown to be capable of detecting the electronic activity of electrogenic cells with greater sensitivity due to the higher charge carrier mobility and chemical stability of CVD graphene.³³ The interaction of CVD graphene films with neurites during their maturation was investigated in a mouse hippocampal culture model.³⁴ Graphene films had excellent biocompatibility, and promoted neurite sprouting and outgrowth. As a consequence, graphene could be a very promising material for cellular-interfaced sensing devices in neuroprosthetic device applications and recording electrogenics activity.^{33,35}

Graphene Films in Biomolecule Investigation Under TEM/HRTEM

Transmission electron microscopy (TEM) and high-resolution transmission electron microscopy (HRTEM) allow the investigation of many different molecules. Existing TEM supports have certain limitations when examining nanoparticles, biomolecules, and biological materials due to interferences coming from the platform. Ultrathin amorphous carbon films (2-3 nm thick) contribute to the overall electron scattering and diminish the contrast of low atomic number specimens.³⁶ This can be overcome by using atomically thin and highly conductive continuous monolayer graphene membranes produced via CVD (**Figure 6**), since they should not interfere with the analysis of the molecules. Graphene-based membranes would be useful not only in static imaging with atomic resolution, but also in the atomic level visualization of dynamic phenomena such as thermally activated desorption, drift, and diffusion processes.³⁷ Graphene was used as an ultrathin support for the direct imaging of the organic capping layers and interfaces attached to gold nanoparticles.³⁶ In another study, graphene flakes were used as TEM support material to study tobacco mosaic viruses (TMVs).³⁸ High contrast was obtained without the need for staining the TMVs.



Figure 6. HRTEM image of a CVD monolayer graphene film ([Aldrich Product Nos. 773697, 773700 and 773719](#)) produced in Graphenea.



Conclusions and Future Perspectives

The versatile chemistry of graphene-based nanomaterials including the capability to conjugate with water soluble and water insoluble active compounds, DNA, proteins, cells, targeting agents, polymers, and even nanoparticles makes them a desirable nanoplatform for future biomedical research. GO has emerged as an extremely interesting material for drug and gene delivery, molecular imaging, and optical biosensor applications. Functionalized GO has been proven to be biocompatible, and when combined with therapeutic agents and targeting strategies, it could lead to improved diagnosis and treatment for a variety of diseases, including cancer. CVD graphene films have emerged as the material of choice for future tissue engineering applications due to their flexibility, atomic thickness, versatility, and unusual properties. The proliferation and differentiation of a number of stem cells have indicated graphene films could become the next scaffolding material. In addition, CVD graphene films were found to be very suitable in FET-type biosensors due to their high sensitivity as a result of their high electronic mobility. These films were also found to be ideal supports for imaging nanoparticles and biomolecules under HRTEM. rGO based electrochemical biosensors were also found to perform very well. However, before graphene and its derivatives can be applied in biomedical/bioelectronic applications, extensive *in vivo* trials will be required.

As a future perspective, recent work has demonstrated the unique capability of graphene to confine light in extreme sub-wavelength spots. This opens up the possibility to develop antenna-based ultrasensitive biosensors using graphene plasmons, where the effective probe volume is on the order of a few tens of nanometers.³⁹ The combination of biology and nanoelectronics could lead to the development of smart neuroprosthetic devices capable of sensing and stimulating at the same time. CVD graphene films interface very well with cells and thanks to their high charge carrier mobility and potential to modulate the charge carrier density, they could have a great future as implantable functional materials.

The fate of graphene and its derivatives in biotechnology is difficult to predict. However, due to their extraordinary characteristics, they have emerged as extremely promising and versatile materials. Nevertheless, the convergence of multiple disciplines will be required for more progress in this research. Ultimately, progress could lead to multifunctional smart materials.

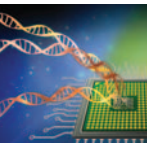
References

- Novoselov, K. S.; Geim, A. K.; Morozov, S. V.; Jiang, D.; Zhang, Y.; Dubonos, S. V.; Grigorieva, I. V.; Firsov, A. A. *Science* **2004**, *306*, 666.
- Mayorov, A. S.; Gorbachev, R. V.; Morozov, S. V.; Britnell, L.; Jalil, R.; Ponomarenko, L. A.; Blake, P.; Novoselov, K. S.; Watanabe, K.; Taniguchi, T.; Geim, A. K. *Nano Lett.* **2011**, *11*, 2396.
- Balandin, A. A.; Ghosh, S.; Bao, W.; Calizo, I.; Teweldebrhan, D.; Miao, F.; Lau, C. N. *Nano Lett.* **2008**, *8*, 902.
- Nair, R. R.; Blake, P.; Grigorenko, A. N.; Novoselov, K. S.; Booth, T. J.; Stauber, T.; Peres, N. M. R.; Geim, A. K. *Science* **2008**, *320*, 1308.
- Lee, C.; Wei, X. D.; Kysar, J. W.; Hone, J. *Science* **2008**, *321*, 385.
- Bunch, J. S.; Verbridge, S. S.; Alden, J. S.; van der Zande, A. M. J.; Parpia, M.; Craighead, H. G.; McEuen, P. L. *Nano Lett.* **2008**, *8*, 2458.
- Wang, Y.; Li, Z.; Wang, J.; Li, J.; Lin, Y. *Trends Biotechnol.* **2011**, *29*, 205.
- Sun, X.; Liu, Z.; Welscher, K.; Robinson, J. T.; Goodwin, A.; Zaric, S.; Dai, H. *Nano Res.* **2008**, *1*, 203.
- Yang, X.; Wang, Y.; Huang, X.; Ma, Y.; Huang, Y.; Yang, R.; Duana, H.; Chen, Y. *J. Mater. Chem.* **2011**, *21*, 3448.
- Zhang, W.; Guo, Z.; Huang, D.; Liu, Z.; Guo, X.; Zhong, H. *Biomaterials* **2011**, *32*, 8555.
- Yang, Y.; Zhang, Y.-M.; Chen, Y.; Zhao, D.; Chen, J.-T.; Liu, Y. *Chem. Eur. J.* **2012**, *18*, 4208.
- Ma, X.; Tao, H.; Yang, K.; Feng, L.; Cheng, L.; Shi, X.; Li, Y.; Guo, L.; Liu, Z. *Nano Res.* **2012**, *5*, 199.
- Feng, L. Z.; Zhang, S.; Liu, Z. *Nanoscale* **2011**, *3*, 1252.
- Chen, B.; Liu, M.; Zhang, L.; Huang, J.; Yao, J.; Zhang, Z. *J. Mater. Chem.* **2011**, *21*, 7736.
- Ryoo, S.-R.; Kim, Y.-K.; Kim, M.-H.; Min, D.-H. *ACS Nano*, **2010**, *4*, 6587.
- Nayak, T. R.; Andersen, H.; Makam, V. S.; Khaw, C.; Bae, S.; Xu, X.; Ee, P. L.; Ahn, J. H.; Hong, B. H.; Pastorin, G.; Ozyilmaz, B. *ACS Nano* **2011**, *5*, 4670.
- Park, S. Y.; Park, J.; Sim, S. H.; Sung, M. G.; Kim, K. S.; Hong, B. H.; Hong, S. *Adv. Mater.* **2011**, *23*, H263.
- Lee, W. C.; Lim, C. H. Y. X.; Shi, H.; Tang, L. A. L.; Wang, Y.; Lim, C. T.; Loh, K. P. *ACS Nano* **2011**, *5*, 7334.
- Peng, C.; Hu, W.; Zhou, Y.; Fan, C.; Huang, Q. *Small* **2010**, *6*, 1686.
- Liu, K.; Zhang, J.-J.; Cheng, F.-F.; Zheng, T.-T.; Wang, C.; Zhu, J.-J. *J. Mater. Chem.* **2011**, *21*, 12034.
- Zhu, S.; Zhang, J.; Qiao, C.; Tang, S.; Li, Y.; Yuan, W.; Li, B.; Tian, L.; Liu, F.; Hu, R.; Gao, H.; Wei, H.; Zhang, H.; Sun, H.; Yang, B. *Chem. Commun.* **2011**, *47*, 6858.
- Chen, M.-L.; Liu, J.-W.; Hu, B.; Chen, M.-L.; Wang, J.-H. *Analyst* **2011**, *136*, 4277.
- Hu, S.-H.; Chen, Y.-W.; Hung, W.-T.; Chen, I.-W.; Chen, S.-Y. *Adv. Mater.* **2012**, *24*, 1748.
- Yang, K.; Zhang, S.; Zhang, G.; Sun, X.; Lee, S. T.; Liu, Z. *Nano Lett.* **2010**, *10*, 3318.
- Chen, W.; Yi, P.; Zhang, Y.; Zhang, L.; Deng, Z.; Zhang, Z. *ACS Appl. Mater. Interfaces* **2011**, *3*, 4085.
- Hong, H.; Yang, K.; Zhang, Y.; Engle, J. W.; Feng, L.; Yang, Y.; Nayak, T. R.; Goel, S.; Bean, J.; Theuer, C. P.; Barnhart, T. E.; Liu, Z.; Cai, W. *ACS Nano* **2012**, *6*, 2361.
- Zhou, M.; Zhai, Y.; Dong, S. *Anal. Chem.* **2009**, *81*, 5603.
- Kuila, T.; Bose, S.; Khanra, P.; Mishra, A. K.; Kim, N. H.; Lee, J. H. *Biosens. Bioelectron.* **2011**, *26*, 4637.
- Unnikrishnan, B.; Palanisamy, S.; Chen, S.-M. *Biosens. Bioelectron.* **2013**, *39*, 70.
- Lu, C.-H.; Li, J.; Liu, J.-J.; Yang, H.-H.; Chen, X.; Chen, G.-N. *Chem. Eur. J.* **2010**, *16*, 4889.
- Ohno, Y.; Maehashi, K.; Yamashiro, Y.; Matsumoto, K. *Nano Lett.* **2009**, *9*, 3318.
- Kwak, Y. H.; Choi, D. S.; Kim, Y. N.; Kim, H.; Yoon, D. H.; Ahn, S.-S.; Yang, J.-W.; Yang, W. S.; Seo, S. *Biosens. Bioelectron.* **2012**, *37*, 82.
- Hess, L. H.; Jansen, M.; Maybeck, V.; Hauf, M. V.; Seifert, M.; Stutzmann, M.; Sharp, I. D.; Offenhäuser, A.; Garrido, J. A. *Adv. Mater.* **2011**, *23*, 5045.
- Li, N.; Zhang, X.; Song, Q.; Su, R.; Zhang, Q.; Kong, T.; Liu, L.; Jin, G.; Tang, M.; Cheng, G. *Biomaterials* **2011**, *32*, 9374.
- Nguyen, P.; Berry, V. *J. Phys. Chem. Lett.* **2012**, *3*, 1024.
- Lee, Z.; Jeon, K.-J.; Dato, A.; Erni, R.; Richardson, T. J.; Frenklach, M.; Radmilovic, V. *Nano Lett.* **2009**, *9*, 3365.
- Westenfelder, B.; Meyer, J. C.; Biskupek, J.; Algara-Siller, G.; Lechner, L. G.; Kusterer, J.; Kaiser, U.; Krill III, C. E.; Kohn, E.; Scholz, F. *J. Phys. D: Appl. Phys.* **2011**, *44*, 055502.
- Nair, R. R.; Blake, P.; Blake, J. R.; Zan, R.; Anissimova, S.; Bangert, U.; Golovanov, A. P.; Morozov, S. V.; Geim, A. K.; Novoselov, K. S.; Latychevskaia, T. *Appl. Phys. Lett.* **2010**, *97*, 153102.
- Chen, J.; Badioli, M.; Alonso-González, P.; Thonggrattanasiri, S.; Huth, F.; Osmond, J.; Spasenovic, M.; Centeno, A.; Pesquera, A.; Godignon, P.; Zurutuza Elorza, A.; Camara, N.; García de Abajo, F. J.; Hillenbrand, R.; Koppens, F. H. L. *Nature* **2012**, *487*, 77.

Graphene

For a complete list of available materials, visit aldrich.com/graphene.

Description	Sheet Resistance (Ω/sq)	Prod. No.
Monolayer graphene film, 1 cm x 1 cm on copper foil, L 1 cm x W 1 cm x thickness (theoretical) 0.345 nm, Monolayer graphene film, L 1.5 cm x W 1.5 cm x thickness 25 μm, Copper foil substrate	600	773697-4EA
Monolayer graphene film, 1 cm x 1 cm on SiO ₂ /Si substrate, L 1 cm x W 1 cm x thickness (theoretical) 0.345 nm, Monolayer graphene film, L 1.25 cm x W 1.25 cm x thickness 525 μm, SiO ₂ /Si substrate	600	773700-4EA
Monolayer graphene film, 1 cm x 1 cm on quartz, L 1 cm x W 1 cm x thickness (theoretical) 0.345 nm, Monolayer graphene film, L 1.25 cm x W 1.25 cm, Quartz	600	773719-4EA



Graphene Oxides

For a complete list of available materials, visit aldrich.com/graphene.

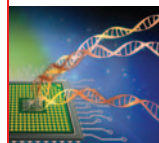
Structure	Description	Prod. No.
	Graphene oxide, dispersion in H ₂ O, 2 mg/mL	763705-25ML 763705-100ML
	Graphene oxide, flakes	763713-250MG

Dyes for Biosensing

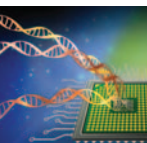
Laser Dyes

For a complete list of available materials, visit aldrich.com/laserdye.

Name	Structure	Purity	Absorption	Prod. No.
2,5-Diphenyloxazole		99%	$\lambda_{\text{max}} = 303 \text{ nm}$	D210404-25G D210404-100G D210404-500G
4-Chloro-7-chlorosulfonyl-2,1,3-benzoxadiazole		97%	$\lambda_{\text{max}} = 324 \text{ nm}$	556505-1G
Carbostyryl 124		99%	$\lambda_{\text{max}} = 350 \text{ nm}$	363308-100MG 363308-500MG
7-Amino-4-methylcoumarin		99%	$\lambda_{\text{max}} = 354 \text{ nm}$ ethanol	257370-100MG 257370-500MG
Coumarin 6		98%	$\lambda_{\text{max}} = 444 \text{ nm}$	442631-1G 442631-5G
2-[4-(Dimethylamino)styryl]-1-methylpyridinium iodide		Dye content: 95%	$\lambda_{\text{max}} = 466 \text{ nm}$	280135-5G
4-(Dicyanomethylene)-2-methyl-6-(4-dimethylaminostyryl)-4H-pyran		Dye content: 98%	$\lambda_{\text{max}} = 468 \text{ nm}$	410497-250MG 410497-1G
3,3'-Diethyloxycarbocyanine iodide		98%	$\lambda_{\text{max}} = 483 \text{ nm}$	320684-1G
Rhodamine 6G		Dye content: 99%	$\lambda_{\text{max}} = 524 \text{ nm}$	252433-250MG 252433-1G
Rhodamine 6G perchlorate		Dye content: 99%	$\lambda_{\text{max}} = 528 \text{ nm}$	252441-250MG 252441-1G



Name	Structure	Purity	Absorption	Prod. No.
Sulforhodamine B, acid form		laser grade, Dye content: 95%	$\lambda_{\text{max}} = 558 \text{ nm}$	341738-1G 341738-5G
3,3'-Diethylthiacarbocyanine iodide		Dye content: 95%	$\lambda_{\text{max}} = 560 \text{ nm}$	173738-250MG 173738-1G
Styryl 9M		Dye content: ~98%	$\lambda_{\text{max}} = 584 \text{ nm}$	417025-1G
Oxazine 170 perchlorate		Dye content: 95%	$\lambda_{\text{max}} = 624 \text{ nm}$	372056-100MG 372056-500MG
Nile Blue A perchlorate		Dye content: 95%	$\lambda_{\text{max}} = 628 \text{ nm}$	370088-1G 370088-5G
1,1'-Diethyl-4,4'-carbocyanine iodide		96%	$\lambda_{\text{max}} = 703 \text{ nm}$ $\lambda_{\text{max}} = 648 \text{ nm}$	D91535-250MG D91535-1G
3,3'-Diethylthiadiazocarbocyanine iodide		Dye content: 98%	$\lambda_{\text{max}} = 655 \text{ nm}$	173754-1G
1,1'-Diethyl-2,2'-dicarbocyanine iodide		97%	$\lambda_{\text{max}} = 707 \text{ nm}$	392197-100MG 392197-250MG
Naphthol Green B		Technical grade	$\lambda_{\text{max}} = 714 \text{ nm}$	N7257-25G N7257-100G
1,1',3,3',3'-Hexamethyln-dotricarbocyanine iodide		97%	$\lambda_{\text{max}} = 740 \text{ nm}$	252034-100MG
3,3'-Diethylthiatricarbocyanine perchlorate		99%	$\lambda_{\text{max}} = 760 \text{ nm}$	389919-100MG 389919-500MG
3,3'-Diethylthiatricarbocyanine iodide		99%	$\lambda_{\text{max}} = 765 \text{ nm}$	381306-250MG 381306-1G
IR-775 chloride		Dye content: ~90%	$\lambda_{\text{max}} = 775 \text{ nm}$	544914-250MG
IR-783		Dye content: 90%	$\lambda_{\text{max}} = 782 \text{ nm}$	543292-250MG

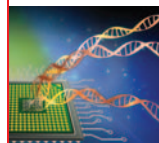


Name	Structure	Purity	Absorption	Prod. No.
IR-806		Dye content: 90%	$\lambda_{\text{max}} = 806 \text{ nm}$	543349-250MG
1,1'-Diethyl-4,4'-dicarbocyanine iodide		Dye content: 90%	$\lambda_{\text{max}} = 814 \text{ nm}$	392200-100MG 392200-250MG
IR-820		Dye content: 80%	$\lambda_{\text{max}} = 820 \text{ nm}$	543365-1G
IR-140		Dye content: 95%	$\lambda_{\text{max}} = 823 \text{ nm}$	260932-100MG
IR-895		97%	$\lambda_{\text{max}} = 895 \text{ nm}$	392375-1G
IR-1048		Dye content: 97%	$\lambda_{\text{max}} = 1048 \text{ nm}$ ethanol	405175-500MG

Chemiluminescent Dyes

For a complete list of available materials, visit aldrich.com/chemilum.

Name	Structure	Purity	Prod. No.
Luminol		97%	123072-2.5G 123072-5G 123072-25G
2,4,5-Triphenylimidazole		98%	T83208-25G
Bis(2-carbopentyloxy-3,5,6-trichlorophenyl) oxalate		$\geq 96.5\%$, titration (by AgNO_3)	393258-5G
9,10-Bis(phenylethynyl)anthracene		97%	264199-1G 264199-5G
Rubrene		$\geq 98\%$	554073-100MG 554073-500MG



Name	Structure	Purity	Prod. No.
Tris(4,7-diphenyl-1,10-phenanthroline)ruthenium(II) dichloride complex		≥95%, HPCE	76886-1MG-F
Tris(4,7-diphenyl-1,10-phenanthroline)ruthenium(II) bis(hexafluorophosphate) complex		≥95.0%, HPCE	85793-1MG-F

Photochromic and Thermochromic Dyes

For a complete list of available materials, visit aldrich.com/chromic.

Name	Structure	Purity	Prod. No.
4,4'-Dipyridyl		98%	289426-5G 289426-25G
Methyl viologen dichloride		98%	856177-250MG 856177-1G
1,1'-Diheptyl-4,4'-bipyridinium dibromide		97%	180858-2G
Benzyl viologen dichloride		97%	271845-250MG 271845-1G 271845-5G
1',3'-Dihydro-1',3',3'-trimethyl-6-nitrospiro[2H-1-benzopyran-2,2'-(2H)-indole]		98%	273619-1G
1',3'-Dihydro-8-methoxy-1',3',3'-trimethyl-6-nitrospiro [2H-1-benzopyran-2,2'-(2H)-indole]		97%	433926-1G 433926-5G
1,3-Dihydro-1,3,3-trimethylspiro[2H-indole-2,3'-[3H] naphth[2,1-b][1,4]oxazine]		≥98.0%, HPLC	322547-250MG 322547-1G

Biotium Kits

Each kit contains 1 vial each of Mix-n-Stain Dye, Mix-n-Stain Reaction Buffer (10x), Mix-n-Stain Storage Buffer, and an ultrafiltration vial.

For a complete list of available kits, visit sigma.com/biotium.

Name	Fluorescence	Prod. No.
Mix-n-Stain™ CF™ 405M Antibody Labeling Kit (50-100 µg)	408 / 452 nm	MX405MS100-1KT
Mix-n-Stain™ CF™ 488A Antibody Labeling Kit (50-100 µg)	490 / 515 nm	MX488AS100-1KT
Mix-n-Stain™ CF™ 555 Antibody Labeling Kit (50-100 µg)	555 / 565 nm	MX555S100-1KT
Mix-n-Stain™ CF™ 568 Antibody Labeling Kit (50-100 µg)	562 / 583 nm	MX568S100-1KT
Mix-n-Stain™ CF™ 633 Antibody Labeling Kit (50-100 µg)	630 / 650 nm	MX633S100-1KT
Mix-n-Stain™ CF™ 647 Antibody Labeling Kit (50-100 µg)	650 / 665 nm	MX647S100-1KT
Mix-n-Stain™ CF™ 660R Antibody Labeling Kit (50-100 µg)	663 / 682 nm	MX660RS100-1KT
Mix-n-Stain™ CF™ 680 Antibody Labeling Kit (50-100 µg)	681 / 698 nm	MX680S100-1KT
Mix-n-Stain™ CF™ 770 Antibody Labeling Kit (50-100 µg)	770 / 797 nm	MX770S100-1KT
Mix-n-Stain™ Biotin Antibody Labeling Kit (50-100 µg)	-	MXBIOS100-1KT



OLED eFabricator

Explore High-performance Materials for Quality Devices

The Organic Light Emitting Diode (OLED) is a high performance optoelectronic device consisting of charge transport and light-emissive layers. Upon applied voltage, the dual carrier injection system of the OLED results in its characteristic light with specific color and device performance, depending on the organic materials employed in the device.

The OLED eFabricator from Aldrich® Materials Science enables you to locate materials to meet your OLED performance requirements by refining the Color, Maximum Luminance, Maximum External Quantum Efficiency, and/or Turn-on Voltage values, offering easy access to Aldrich's extensive portfolio of high-quality small-molecule organic materials and polymers for OLEDs and PLEDs.

Find the materials you need for OLED construction by refining the values in the fields below:

AVAILABLE COLOR FAMILIES		UNIQUE PROPERTIES RANGE SELECTORS	
R Red <small>(Shown)</small>	G Green <small>(Shown)</small>	B Blue <small>(Hidden)</small>	
		Max. LUM Max. Luminance (Cd/m ²)	100 — 1,000 - 26,000 Cd/m ² — 50,000
		Max. EQE External Quantum Efficiency (%)	0.03 — 5 - 17% — 19
		TOV Turn-On Voltage (V)	2 — 3 - 6 V — 10

SELECTION INFORMATION 42 Configurations Available in 3 Colors: Red, Orange Red, Green

GREEN	CATHODE (-) <u>Al/LiF</u>	REFERENCES Appl. Phys. Lett. 99, 153303 (2011)
Max. LUM 20,000 Cd/m²	ETL <u>BPhen</u>	
Max. EQE 1.2%	EML <u>Alq₃</u>	
TURN-ON V. 2.8 V	HTL <u>NPD (NPB)</u>	
LIFETIME n/a	ANODE (+) <u>MoO₃/ITO</u>	



With the OLED eFabricator, you can easily locate OLED materials based upon performance requirements aldrich.com/oledtool